Monochromatic molecular absorption coefficients for use in calculations of stellar opacity

MONOCHROMATIC MOLECULAR ABSORPTION COEFFICIENTS
FOR USE IN CALCULATIONS OF STELLAR OPACITY

A Thesis by

Kari Lynn Ehrmann

Bachelor of Science, Wichita State University, 2016

Submitted to the Department of Math, Statistics and Physics
and the faculty of the Graduate School of
Wichita State University
in partial fulfillment of
the requirements for the degree of
Master of Science

May 2018

MONOCHROMATIC MOLECULAR ABSORPTION COEFFICIENTS

The following faculty members have examined the final copy of this thesis for form and content, and recommend that it be accepted in partial fulfillment of the requirements for the degree of Master of Science, with a major in Physics.

Jason W. Ferguson, Committee Chair

Elizabeth Behrman, Committee Member

Doug English, Committee Member

DEDICATION

To my parents, Robin and Bryan, I am truly grateful for your continued support, for without it, I would not have had the opportunity to finish my education. To my children, Kiara, Avery and Harper, thank you for being the bright part of my days. To my sister, Kallie, you were a huge stress reliever just by listening, thank you for being there when I needed it. Finally, to my husband and best friend, Chris, who held me up through the tough times. You are everything I could ever ask for. Thank you for being my strength to keep moving forward. It has been a journey for us all.

We are all connected; To each other, biologically. To the Earth, chemically. To the rest of the universe, atomically.

— Neil deGrasse Tyson

ACKNOWLEDGEMENTS

I would like to thank my advisor, Jason Ferguson, for the continued help and wealth of knowledge throughout this project. I appreciate all your words of encouragement. I would also like to recognize my colleagues in the Society of Physics Students. It has been a wonderful opportunity to know each and every one of you and I will cherish the bond that we have created over the many years together. Thank you all. I also would like to thank the group of graduate students I had the chance to get to know in my last year here. You kept me laughing through every exam and homework assignment. To my friend, Kaitlin Patterson, thank you for being such an awesome friend. I appreciate all the times you were there for me. I would also like to recognize my friend, Alan Cedeno. I enjoyed our fun and interesting conversations throughout grad school. I hope you achieve everything you set out for. Lastly, I would like to thank Reed Bowles, for being a great friend over the years. I know you'll be an incredibly talented scientist and future professor.

ABSTRACT

In order to fully understand stellar structure, it is necessary to know the opacity, as it influences the behavior of radiative transfer within the stellar interior. Opacity plays an important role in the onset of convection as well as driving stellar winds in cool stars. Opacity is the interaction of light with the surrounding medium, with major contributors being atoms, molecules and grains. Tables of average opacity values are highly dependent on the composition and if any changes are made, a whole new set of tables must be recalculated. Using molecular line lists, a computer program was written to calculate the bound-bound transition cross-section absorption coefficients for eight different molecular species, including C_2, CH, CN, CO, C_2H_2, H_2O, HCN, and TiO. Molecular line lists, like H_2O, consist of hundreds of millions of lines of data that slow down the process of calculation. Since the frequency specific opacity is dependent on temperature, the molecular absorption coefficients must be calculated for each and every temperature. This project computed cross-sections computed for a range of temperatures, $log\ T[K] = 2.8 - 4.0$. Molecules were examined thoroughly at $log\ T[K] = 3.0$. This research allows for an update in mean opacity tables based upon each molecular species and its abundance, providing necessary improvements in the computation of mean opacity tables used in stellar interior models.

TABLE OF CONTENTS

Chapter Page

TABLE OF CONTENTS (continued)

LIST OF TABLES

LIST OF FIGURES

LIST OF SYMBOLS

κ_R	Rosseland Mean Opacity
κ_P	Planck mean opacity
B_ν	Planck Function
ρ	Gas Density
L	Luminosity
r	Stellar Radius
a	Radiation Density Constant
π	Pi
e	Charge of the Electron
m	Molecular Mass
m_e	Mass of the Electron
c	Speed of Light
g	Statistical Weight
f	Oscillator Strength
T	Gas Temperature
Q	Partition Function
E_0	Lower Level Energy

ν	Frequency
ν_0	Frequency of Lower Level
ϕ	Normalized Broadening Function
Δ_ν	Doppler Width
ξ	Microturbulent Velocity
n_j	Number Density
σ_{bb}^{abs}	Bound-Bound Absorption Coefficient
k_B	Boltzmann Constant
h	Planck Constant
n	Lower Level
m	Upper Level
E_{nm}	Energy Level
A_{nm}	Einstein A Coefficient
B_{nm}	Einstein B Coefficient

Chapter One

1 Introduction

Stars have long been admired for their brilliance and apparent simplicity. For decades, astrophysicists have attempted to model the life of a star through the use of computer simulation, which are becoming more and more complex. In order to correctly replicate the life of a star, the proper composition and basic structural equations must be considered. Computation of a star's development involves many constituents, including the use of tables of mean opacity, a small component that often makes significant contributions to the path of a star's lifetime. These tables are interpolated as the composition of the star evolves. However, since the mean opacity changes when the composition of a star changes, those original mean opacity tables become inaccurate over the life of the star. Therefore a quick computational tool for calculating mean opacities is needed. This thesis is a small step towards creating a faster, more accurate representation of mean opacity tables, leading to more accurate stellar models.

1.1 Radiative Transfer and the Mean Free Path of a Photon

Small scale contributions to the internal functions of a star allow a greater understanding of the process of stellar evolution. The main stellar structure equations each describe a component of the comprehensive structure of the star. There are four major stellar structure equations: hydrostatic equilibrium, mass continuity, radiative transfer and conservation of energy. Each governing equation illustrates a framework for the anatomy of a star. Of the stellar structure equations, the radiative transfer equation characterizes how the total radiative energy is transferred through a spherical shell,

$$\frac{dT(r)}{dr} = -\frac{L(r)\kappa(r)\rho(r)}{4\pi r^2 4acT(r)^3}. \tag{1}$$

The temperature gradient, $\frac{dT}{dr}$, is directly proportional to the luminosity, L, total opacity, κ, and density, ρ, each with a dependence on radius, r. Within the denominator, there is a relation to the spherical surface area, $4\pi r^2$, the radiation density constant, a, speed of light, c, and temperature, T. The equation of radiative transport shows a direct relationship to the total opacity, κ. Opacity pertains to the radiative absorption capacity of stellar material. This implies a correlation of how photons travel and interact through the material of the star [32].

The interaction of light with matter involves absorption-emission, scattering and extinction of photons. These processes affect the mean free path of a photon as it wanders towards the outer layers of the star. The mean free path of a photon describes the distance that a photon can travel before interacting with the surrounding medium. As a photon travels, it is constantly interrupted with the neighboring atoms or molecules. This interaction not only alters the photon's path, but redistributes its energy[9].

1.2 Absorption Processes

The absorption of a photon is the process that essentially eliminates a photon of specific energy from an incident beam of light [29]. This absorption process causes an exchange of energy, from the photon to the thermal kinetic energy of the surrounding medium. In this way, absorption is closely related to the local thermodynamic properties of the gas [28]. All of the following processes produce a continuum opacity, except bound-bound, which produces a line opacity.

1.2.1 Free-Free

Free-free absorption is a scattering process where a photon is absorbed by a free electron near an ion, which increases the electron's kinetic energy. This involves a change in the electron's motion from one free state to another. It can still be associated with a nucleus, without being bound to it [29]. The free-free absorption signifies the fact that the electron was free before and after the absorption occurs [28].

1.2.2 Bound-Free

Bound-free absorption is also known as photoionization. In this case, a photon is absorbed by the atom and ionizes the bound electron, which is freed. During this process, the photon is consumed, and its energy feeds into the electron's kinetic energy. Eventually this energy increases the overall thermal pool, causing an increase in elastic collisions of the electron. The increase in the thermal pool indicates a distribution of thermal velocities [28].

1.2.3 Bound-Bound

Absorption via spectral lines occur when an electron, bound to an atom with discrete energy levels, transitions from an initial energy level to higher energy level. Such distinct transitions are named bound-bound transitions and correspond to an absorption of a single frequency [9]. The difference in energy levels, from initial to final, determines the magnitude of energy and as a result, the frequency of the absorbed photon can be calculated [29]. After the absorption process, the atom then follows a de-excitation procedure. This can take place either spontaneously or through an inelastic collision with another particle. If collisions are involved, the additional kinetic energy from the previous absorption then contributes to the thermal pool. Therefore the photon is destroyed by collisional de-excitation [28].

The reverse process occurs when the electron emits a photon through either collisional or spontaneous de-excitation. This removes energy from the thermal pool. The electron transitions to a lower energy level, creating a distinct frequency due to the emission of the photon [29].

1.2.4 Scattering

The scattering process occurs when a photon is deflected by an electron. The interaction could potentially be through an absorption-emission process, or simply a scattering center. After the interaction, the photon is left with an altered direction and somewhat modified energy. This differs from the free-free absorption process, where the electron gains the kinetic energy of the photon. In this case, the energy of the photon does not become converted to kinetic energy and also does not affect the thermal energy [28].

1.2.5 Extinction Coefficient

The extinction coefficient describes the total removal of energy from the radiation field, also known as the opacity. The calculation of the extinction coefficient gives an explanation of the distance the photon propagates before it is removed. The extinction coefficient is the product of absorption cross-sections and number density of absorbers summed over all states that interact with photons of a certain frequency, ν [28]. In a broad sense, the extinction coefficient can be regarded as the total absorption coefficient.

1.3 Absorption Profile

The absorption profile becomes influenced by the probabilities of transition between energy levels. The spectral line for each corresponding absorbed frequency becomes broadened due to the perturbations of nearby atoms and ions. This distribution of frequencies create an absorption profile, ϕ_ν, that must be normalized such that $\int \phi_\nu d\nu = 1$ [28]. A more thorough discussion of ϕ_ν appears in Chapter 2.

1.3.1 Energy Levels and Transition Probabilities

Within the bound-bound absorption process, the change in energy levels reveals the frequency at which a photon was absorbed, $h\nu_{nm} = E_m - E_n$, where Planck's constant, h, and the frequency, ν, is directly related to the change in energy levels, E_{mn}. The subscripts define upper and lower levels, m and n, respectively. The probability that a transition will occur is also an essential component to understanding the overall absorption. These probabilities are given through the Einstein transition coefficients, A_{mn}, and B_{nm}[29]. The Einstein B coefficient depicts the likelihood of a stimulated transition. This transition can be applied to either an absorption or emission process, B_{mn} or B_{nm}, respectively. The Einstein A coefficient specifically portrays spontaneous emission process, A_{mn}. The Einstein B coefficient can be associated to the Einstein A coefficients through a set of Einstein relations based on the rates of absorption and emission in thermodynamic equilibrium [28]. These relations can be linked to an f-value, or oscillator strength of the transition, given in the following equation (2) as seen in reference [11].

$$f_{mn} = \frac{c^3 m_e}{8\pi^2 e^2 \nu_0^2} \frac{g_m}{g_n} A_{mn}. \tag{2}$$

Constants include the speed of light, c, mass of the electron, m_e, followed by π, the charge of the electron, e, and the initial frequency, ν_0. This is accompanied by a ratio of statistical weights of the upper level to the lower level, g_m and g_n [11]. The statistical weight of an energy level takes into account the quantum mechanical effects of degenerate energy states [29].

1.3.2 Doppler Broadening and Microturbulent Velocity

The absorption profile naturally forms steep peaks, though there are many mechanisms that cause ambiguity in the full width of the spectral lines. This leads to a necessity to incorporate the broadening of the absorption profile. Though line broadening effects can be observed through natural damping or pressure broadening, the influence of thermal Doppler effects is incorporated into the line profile [28]. Line broadening due to the Doppler effect is mainly caused by the thermal motions of atoms and ions. This turbulence must be included in the calculation of the Doppler half width because of its large contribution, as discussed in Chapter 2.

1.4 Mean Opacity

In order to find the monochromatic absorption opacity due to the absorption sources, the calculation must include all contributions from each source, namely

$$\kappa(\nu) = \kappa_{atomic} + \kappa_{molecular} + \kappa_{dust}. \tag{3}$$

This coefficient includes the product of the absorption cross-section and the number density, summed over all states that interact with photons of frequency, ν [28]. The opacity, κ, of the jth absorption source is given by the number density, n_j, over the gas density, ρ. The monochromatic cross-section of the jth process is designated as σ [26] The term $\frac{n_j}{\rho}$ relates to the abundance of each source

$$\kappa_j^{abs}(\nu) = \frac{n_j}{\rho}\sigma_j^{abs}(\nu). \tag{4}$$

Opacity calculations are frequency dependent functions of density and temperature. A mean or frequency averaged, opacity is necessary for the calculation of the radiative transfer equation (1). If the radiative transfer equation remains a function of frequency, computation becomes extremely lengthy and nearly impossible. There are two types of mean opacity to consider.

1.4.1 Planck Mean Opacity

The Planck mean opacity, in equation (5), is a straight mean that weights more heavily the frequencies that produce the greatest opacity. This calculation is significant in the outer layers of a star when the optical depth is small and the mean free path of the photon is very long [28]. Using the Planck Function, given by $B_\nu(T)$, as a weight factor, the Planck mean opacity is

$$\kappa_P(\rho, T) = \frac{\int\limits_0^\infty \kappa(\nu) B_\nu(T) d\nu}{\int\limits_0^\infty B_\nu(T) d\nu}. \tag{5}$$

Within this equation is the sum of all contributions to opacity and the Planck Blackbody function, $\kappa(\nu)$, and B_ν, respectively.

1.4.2 Rosseland Mean Opacity

The Rosseland mean opacity, in equation (6), describes a harmonic mean of the monochromatic opacities. This averaging function weights more heavily the regions where the opacity is lowest. This is a standard calculation for the absorption in the interior of the star where the mean free path of the photon is very short. The absorption of weak lines are thermally broadened by collisions, and must be taken into account [29]

$$\frac{1}{\kappa_R(\rho,T)} = \frac{\int\limits_0^\infty \frac{1}{\kappa(\nu)} \frac{\partial B_\nu}{\partial T} d\nu}{\int\limits_0^\infty \frac{\partial B_\nu}{\partial T} d\nu}. \tag{6}$$

The calculation of the Rosseland mean opacity, as seen in equation (6), is discussed in the results of Section 5.1.

Chapter Two

2 Molecular Absorption Cross-Section

Molecules introduce an additional complexity to the fundamental absorption processes. The structure of the molecule plays a key role in the energy transitions. There are three distinct components that factor into the possible energy transitions: the rotational, vibrational and electronic energy transitions. This allows a spread in absorption lines, shaping the bands of each molecule, as will be discussed in Chapter 4. This produces a substantial number of possible transition levels, as shown in table (2). Every term affects the probability of transition and each condition leads to millions of transition energy states. Due to the the extensive transition lines lists, the calculation of molecular absorption cross-sections become extremely computationally intensive.

2.1 Cross-Section Calculation

The absorption coefficient cross-section refers to a single molecular absorption source and considers the probability of each bound-bound transition. The cross-section is frequency and temperature dependent:

$$\sigma_{bb}^{abs}(\nu) = \frac{\pi e^2}{m_e c}\frac{gf}{Q(T)}e^{-\frac{E_0}{k_b T}}(1 - e^{\frac{-h\nu_0}{k_b T}})\phi(\nu). \quad (7)$$

The first segment includes constants such as π, e, charge of the electron, m_e, mass of the electron and c, the speed of light. The equation continues with a gf value, where g is the statistical weight and f is the oscillator strength of the transition. The statistical weight depends on the element, the bound level and the wavelength of the photon [29]. This gives insight on the probability of how likely a transition is to occur. Below that is the temperature dependent partition function *Q(T)*, which is needed for each molecule. This is followed by the Boltzmann distribution function, which gives rise to yet another probability that is dependent on the difference of energy states of a transition. After the Boltzmann distribution is a stimulated emission correction factor in parentheses.

The last term in equation (7) is the normalized broadening function, $\phi(\nu)$, takes into consideration the line broadening due to collision-induced thermal broadening.

$$\phi(\nu) = \frac{1}{\Delta_\nu \sqrt{\pi}} e^{-(\frac{\nu-\nu_0}{\Delta_\nu})^2}. \tag{8}$$

The frequency displacement from the line-center, $(\nu - \nu_0)$, as seen in the exponent is measured in Doppler widths, $\Delta\nu$. This difference in frequency allows a development for the Doppler profile, in equation (9), which includes a dominant contribution from microturbulent velocities, ξ. The microturbulent velocities account for a thermal broadening of the profile, and are set at a standard parameter value of 2.5 $km\ s^{-1}$

$$\Delta_\nu = \frac{\nu_0}{c}\sqrt{\frac{2k_bT}{m} + \xi^2}. \tag{9}$$

Each individual transition cross-section is then summed over all lines to find the total contribution of each molecule:

$$\sigma_{mol}^{abs}(\nu) = \Sigma_{lines}\sigma_{mol}^{abs}(\nu). \tag{10}$$

Chapter Three

3 Objectives and Techniques

An algorithm was developed using FORTRAN to calculate the monochromatic absorption cross-section for bound-bound transitions, in equation (7), established from the ÆSOPUS [26] paper. The eight molecules included C_2, CH, CN, CO, C_2H_2, HCN, H_2O and TiO. For each molecule, data tables were created for 9279 frequencies over twelve different temperatures. The temperatures ranged from $log\ T[K] = 2.8$ to 4.0 in increments of $log\ T[K] = 0.1$, ranging from $630K$ to $10,000K$. This was based on the formalism in the AF94 paper, now referenced as Atop hereafter [1].

The primary goal of this research was to update the original Atop code, in order to shorten computation time and provide opacity tables at a wider range of density, temperature and compositions. These quickly computed mean opacity tables are extremely useful in stellar evolution codes. It would eliminate the need to interpolate mean opacities in stellar evolution codes and provide specific values necessary to compute the stellar structure equations. The molecular line absorption coefficients calculated here with more recent data, can then be included to help create a more accurate version of the Atop code. The opacity tables would then be updated with a comprehensive list of very important molecular absorbers. The chosen molecules in this study are used because of their significant impact in opacity. This in turn becomes an important factor when modeling stellar evolution at different carbon-oxygen ratios. The newer monochromatic absorption cross-section data was compared to the original Atop code as well as the more recent Phoenix code for each molecule [12]. The most accurate data source from each molecule will be included in the Atop code opacity model. Results and further discussion can be found in Chapter 6.

3.1 Data Sources

Molecular line data was collected from three predominant sources. Each source was compiled using distinct formatting inputs and evaluated graphically as well as with an analysis in an opacity calculation. The initial source was from the original compilation from Atop and was used as a comparison in the majority of analysis.

3.1.1 Atop

The data from the Atop code was used in the compilation of Rosseland opacity over a range of temperatures and densities. The absorption of atomic and molecular lines were computed monochromatically. The full description of computations can be found in the AF94 paper [1]. Atop is the code that produced the original opacity tables for a collection of densities and temperatures.

3.1.2 Phoenix

The Phoenix code [12] was an update to the previous opacity code from Atop. The improved program included many additional molecular species, as well as updated optical constants for dust. The formalism for the Phoenix code is thoroughly discussed in the F05 paper. Rosseland Mean Opacities calculated in the following chapters were calculated with the use of the Phoenix code.

3.1.3 ExoMol

ExoMol is a collection of molecular line lists and transition files functioning as a database for usage in modeling brown dwarf models and cool stars. It also includes uses for spectroscopy of stellar atmospheres and stellar opacity models. The majority of sources also include partition functions calculated from various individual groups [34]. ExoMol is a significant source of material for the majority of molecules that were analyzed. ExoMol data is formatted to include line transitions, energy levels, Einstein A coefficients, statistical weight levels. Many of the sources also included partition function lists over a wide range of temperatures.

3.1.4 HITRAN

HITRAN is an online compilation of molecular line lists with adjustable parameters. It uses a database from HITEMP, or high-temperature spectroscopic absorption parameters. This database is supported by the Atomic and Molecular Physics Division at the Harvard Smithsonian Center for Astrophysics. The online database incorporates partition functions for a full range of temperatures, up to $10,000$ K [16].

3.1.5 VizieR

VizieR is a catalog compilation created by CDS (Centre de Donnés astronomiques de Strasboug) and ESA-ESRIN (Information Systems Division) to create an online database of astronomical catalogs. It includes $17,190$ catalogs of accessible data tables. Multiple partition function data tables were extracted from VizieR. Partition functions from VizieR were listed for 42 temperatures ranging from 0 to $10,000K$ [6].

3.2 Partition Functions

Partition functions were obtained from ExoMol, HITRAN, and VizieR. Originally the specific value of $Q(T)$ was found for each value of $log\ T[K] = 2.8$ to $log\ T[K] = 4.0$ in increments of 0.1 using a finite difference method. In order to increase efficiency in the code and decrease the run time, every partition function was fitted with a third or fourth-order polynomial. This choice was dependent on the fit of the polynomial to each partition function of each molecule. In cases with multiple partition function lists, the source was chosen based upon the accuracy of the fitted function.

With seven of the molecules, a fitted function was used. The finite difference method was used in the calculation of the partition function for C_2H_2, due to the high errors in the fitted function. Below is a table of coefficients for the fitted function of each molecule. The method used in determining the fitted function was based on the Shomate equations[10].

$$a + b\theta + c\theta^2 + d\theta^3 + e\theta^4 \tag{11}$$

where

$$\theta = \frac{T[K]}{1000} \tag{12}$$

Table 1: **Fitted Partition Functions**

Molecule	a	b	c	d	e
C_2	-37.3285	261.1606	534.7567	40.8371	1.0654
CH	11.131	165.24	17.789	8.8349	
CN	3.5757	643.88	111.41	26.705	
CO	40.153	218.72	108.51	1.7745	
HCN	341.49	-361.35	6423.5	1261.3	2255.4
H_2O	-66.5	716.84	371.53	118.46	90.663
TiO	-82.731	4100.6	5652.4	-113.11	46.873

Chapter Four

4 Molecule Review

Specific authors for each molecular line list will be discussed followed by a graphical analysis of each source. All molecules were analyzed at a set temperature of *log* $T[K] = 3.0$. Each graph will show the logarithm of the molecular cross-section, logarithm of σ, over a range of wavelengths in Angstroms, Å. Table (2) shows a concise list of all molecular line data and their corresponding source. The partition function source is also included for each molecule.

Table 2: **Molecular Sources**

Molecule	Line Lists	Number of Transitions	Partition Function
C_2	1	1,494,062	
	9	1,367,097	20, 24
	17	47,570	
C_2H_2	2	10,000,000	
	26	22,866	26
CH	1	61,856	
	11	43,999	21, 24
	21	53086	
CN	3	2,200,000	
	12	1,114,335	19
	11	605,816	
	22	195,120	
CO	4	37,720	
	13,14,15	19,204	25
	11	199,040	
	25	131,859	
HCN	7	10,000,000	
	23	34,418,408	23
H_2O	5, 6	20,000,000	
	16	6,139,498	
	17	307,695,617	
	21	558,095,683	
TiO	8	12,312,080	
	19	2,050,779	24
	18	32,190,772	

References: **Atop**: (1) Sharp 1984; (2) Jørgensen 1993; (3) Jørgensen & Larsson 1990; (4) Goorvitch & Chackerian 1994; (5) Jørgensen & Jensen 1993; (6) Jørgensen, Jensen and Sørensen 1994; (7) Jørgensen et al. 1985; (8) Jørgensen 1994a; **Phoenix**: (9) Huber & Herzberg 1979; (10) HITRAN 1992; (11) Kurucz 1993; (12) Jørgensen & Larsson 1990; (13) Goorvitch 1994; (14) Goorvitch & Chackerian 1994a; (15) Goorvitch & Chackerian 1994b (16) Allard et. al. 1994; (17) Partridge & Schwenke 1997; (18) Schwenke & Allard 2000; (19) Jørgensen et al. 2001; **ExoMol**: (20) Brooke et al. 2013; (21) Masseron et al 2014; (22) Brooke et al. 2014; (23) Harris et al. 2006; **VizieR**: (24) Barklem & Collet 2016; (25) Goorvitch 1995; **HITRAN**: (26) HITRAN database 2016

4.1 C_2

This molecule was analyzed using three main sources of molecular line transition lists. The first source was from a previously calculated table using data from Sharp 1984 from the ATOP code. A second data set came from the PHOENIX code, using transitions and energy lists from Huber & Herzberg 1979. A newer external source was found through the ExoMol website. This database included molecular line lists and a partition function for temperatures ranging from $0 - 3000K$ from Brooke et al. 2013. After an initial analysis, a second partition function was found from VizieR, compiled by Barklem & Collet 2016, which contained a broader range of temperatures.

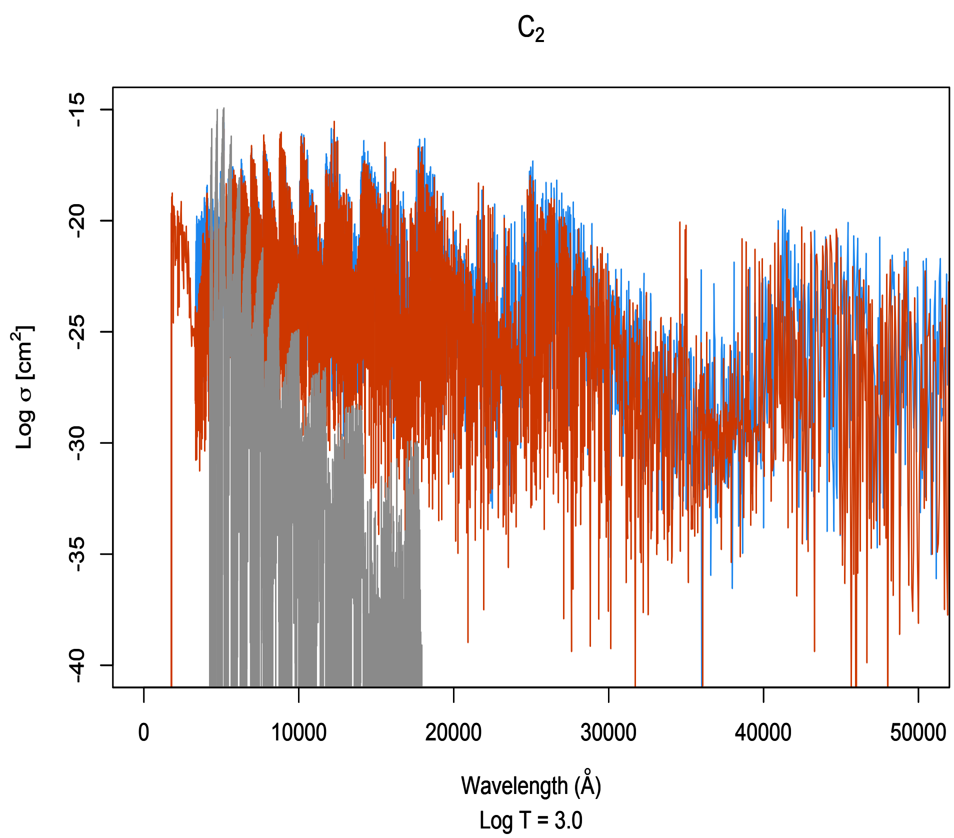

Corresponding colors: ATOP - **Blue**; PHOENIX - **Red**; ExoMol - **Grey**

Figure 1: C_2: Full Scale

The full scale graph shows an agreement between each of the sources. Data sources are ordered as follows; PHOENIX, ATOP, and ExoMol, in red, blue and grey, respectively. PHOENIX and ATOP cross-sections are confined between the range of -40 to -15, though ExoMol falls well below the low limit. The ExoMol source behaves in this way due to the reduced transition line list in comparison to the other sources. Though the peaks from each source coincide very closely, the ExoMol data decreases much more quickly. This behavior will lead to less of an impact in the overall calculation of the Rosseland opacity. Within the more focused graph, the C_2 Swan bands are clearly shown between 4250 and 6000 Å. Between 6000 Å and $10,000$ Å in the focused graph, there is a clear distinction in the shape of the ExoMol data in comparison to the PHOENIX and ATOP.

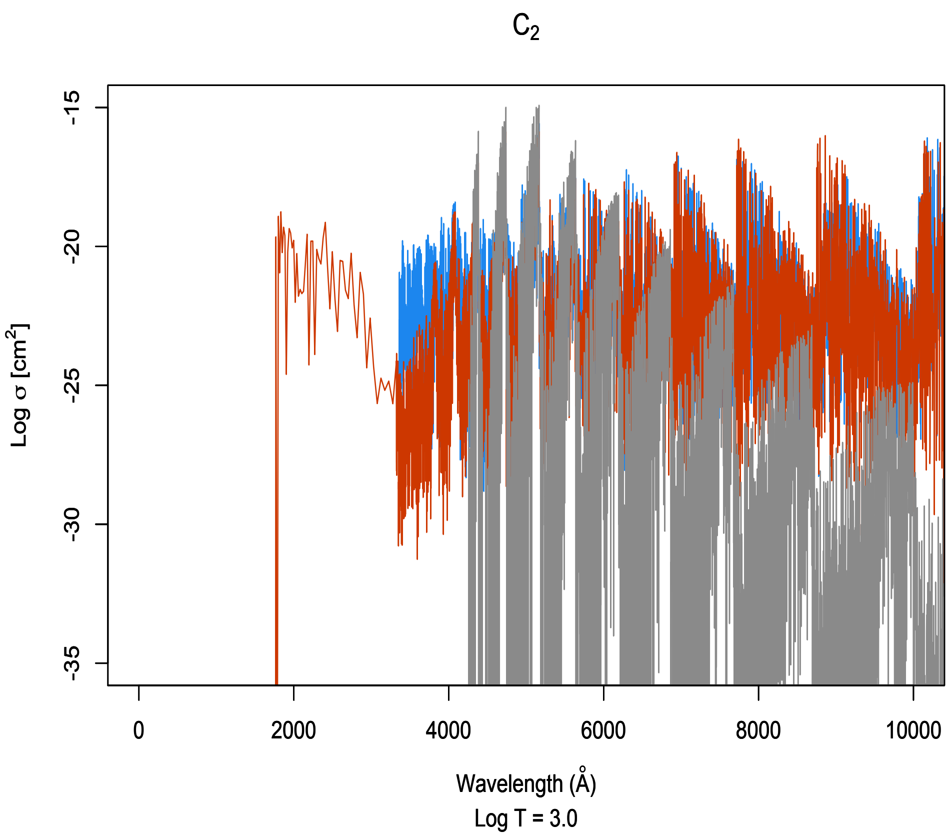

Corresponding colors: ATOP - **Blue**; PHOENIX - **Red**; ExoMol - **Grey**

Figure 2: C_2: Focused

4.2 CH

This molecule was analyzed using two sources of molecular line transitions from PHOENIX and ExoMol, and compared to a previously calculated cross-section from ATOP. Data from ATOP originally came from Sharp 1984. Transition line lists from the PHOENIX code originally came from Kurucz 1993. The data from the ExoMol website was sourced from Masseron et al. 2014. A partition function was used from Masseron et al. 2014 from the ExoMol website as well as from VizieR from Barklem & Collet 2016.

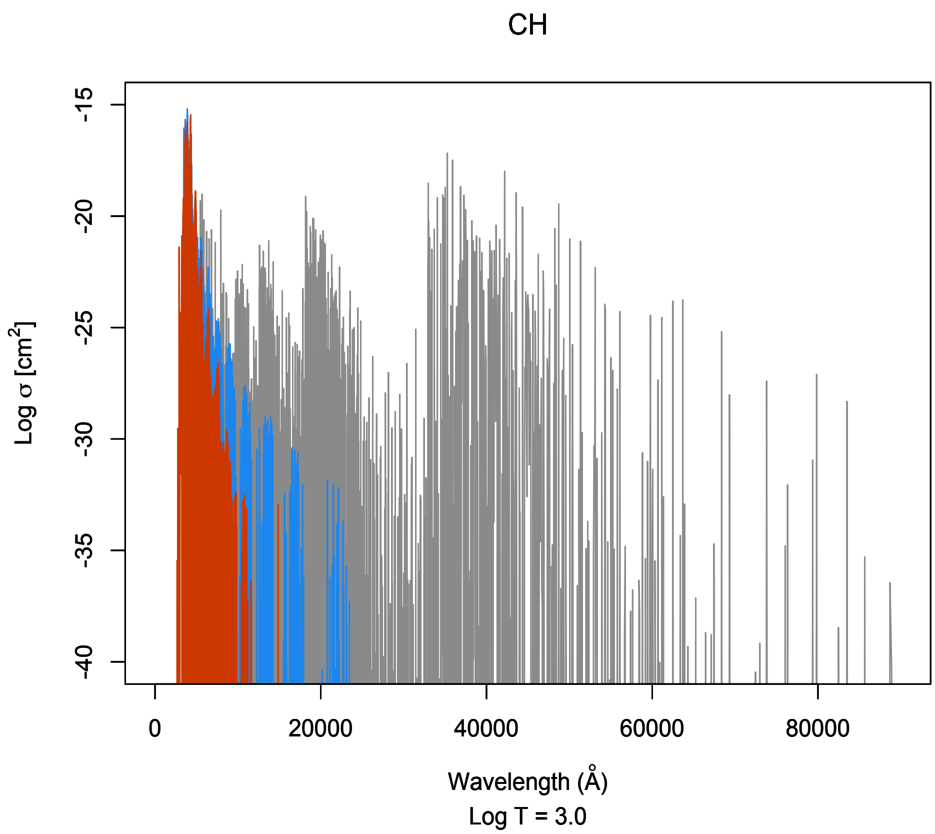

Corresponding colors: ATOP - **Blue**; PHOENIX - **Red**; ExoMol - **Grey**

Figure 3: CH: Full Scale

In the full scale graph, the bands of CH are aligned between the sources, though there are slight differences in the magnitude of $log\ \sigma\ [cm^2]$ as the wavelength increases. The lines for each source continue below the $log\ \sigma[cm^2] = -60$. This behavior can be explained due to the limited number of transitions, from each source. The ExoMol source does produce bands through $80,000$ Å, where the other sources end around $20,000$ Å. In the focused graph, the first four major bands near 4000 Å correlate well. With the agreement between the sources, the opacity calculation can be expected to be similar, however, ATOP remains slightly higher than the others.

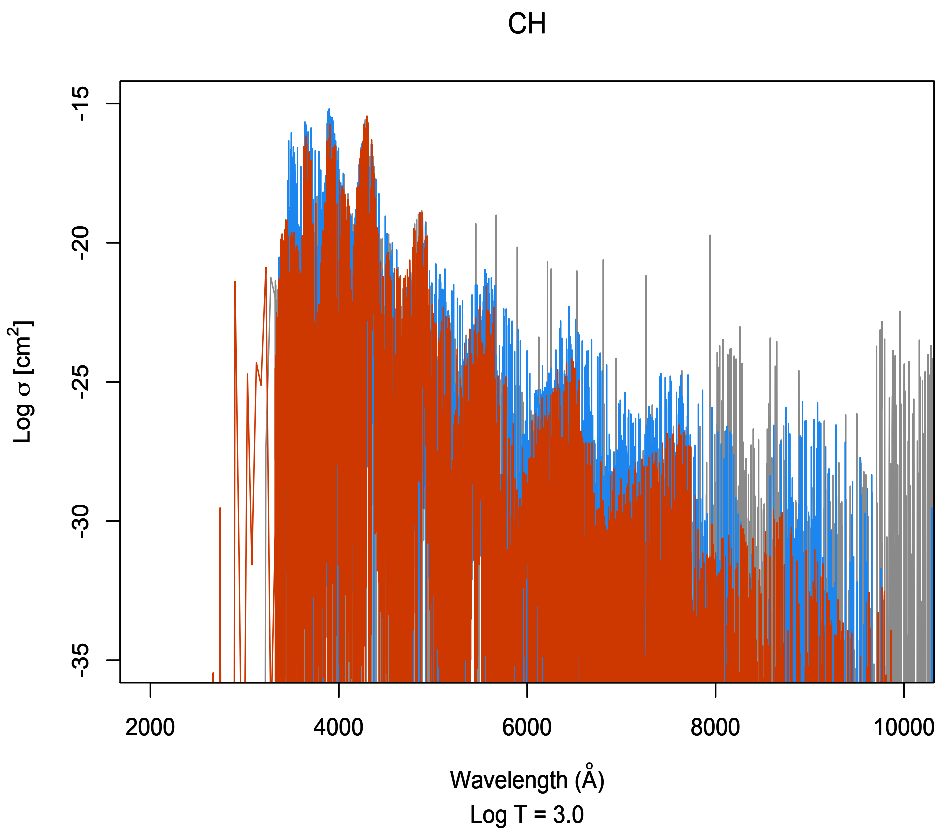

Corresponding colors: ATOP - **Blue**; PHOENIX - **Red**; ExoMol - **Grey**

Figure 4: CH: Focused

4.3 CN

A total of four sources were found for CN. The original cross-section table was used from Atop, as well as two sources from Phoenix. The most recent source was found on the ExoMol website, using transition line lists from Brooke et al. 2014. Two sources came from Atop, from Jørgensen & Larsson 1990, as well as from Kurucz 1991. Phoenix provided one other data source from Kurucz 1993. The partition function used was included with the molecular line lists from ExoMol by the same author.

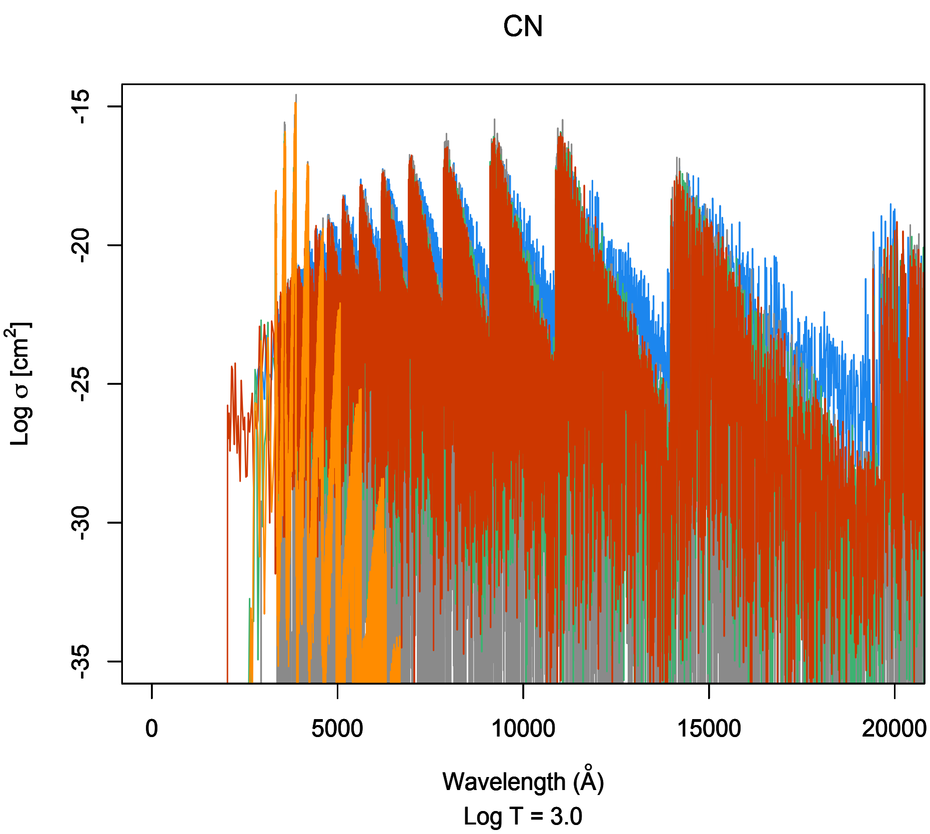

Corresponding colors: Atop - **Blue**; Atop Kurucz Blue/Violet bands - **Orange**; Phoenix Jørgensen - **Red**; Phoenix Kurucz - **Green**; ExoMol - **Grey**

Figure 5: CN: Full Scale

The bands of CN correlate well through each of the four data sets. Though the Jørgensen data is the same with the ATOP and PHOENIX source, the results are slightly different. Since only one was compiled through the algorithm, inconsistencies in calculation could have been involved. The bands of the ATOP source continue to be a few orders of magnitude higher than the rest in the slope of each peak. From the focused graph, it is apparent the four sharp peaks below 5000 Å. These peaks correspond with the Blue-Violet bands of CN, as shown by the orange data from Kurucz. It is important to note the distinction between line lists. In the following page will be the sources separated in three figures (7, 8, 9) in order to display the variation between newer sources of data and the original ATOP.

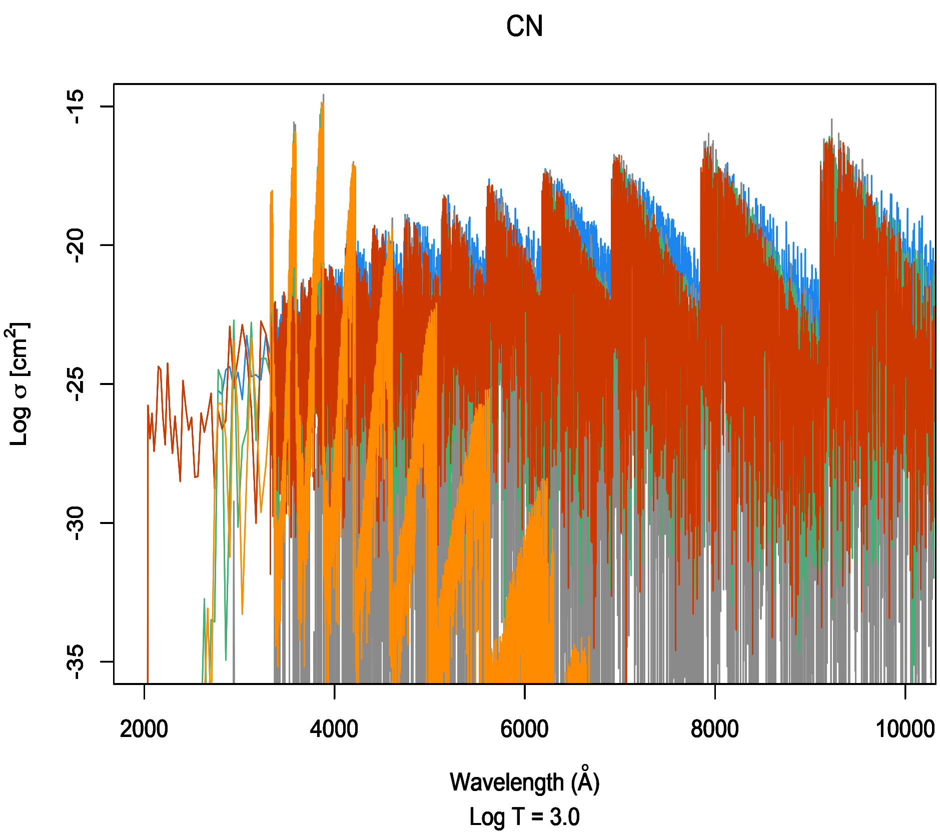

Corresponding colors: ATOP - **Blue**; ATOP Kurucz Blue/Violet bands - **Orange**; PHOENIX Jørgensen - **Red**; PHOENIX Kurucz - **Green**; ExoMol - **Grey**

Figure 6: CN: Focused

In figure (7), the ATOP data that includes the Blue-Violet lines, is paired with the ExoMol data. It is clear that ATOP is continuously greater in magnitude in comparison to ExoMol. The ExoMol data includes a comprehensive line list that includes the initial peaks in the Blue-Violet system. For the following figure of ATOP with Jørgensen, figure (8), it is evident that the Jørgensen line list does not include the preliminary peaks. The differences in magnitude of Jørgensen in comparison to ATOP, appear very similar to the distinction in magnitude of ExoMol and ATOP. In the final split figure, (9), Kurucz, in green, is coupled with ATOP. The Kurucz line list appears very similar to the Jørgensen data, with the addition of the Blue-Violet system. The initial peaks of Kurucz show a better fit to the ATOP peaks than the ExoMol data. Overall the magnitudes of ATOP clearly exceed each of the data sources.

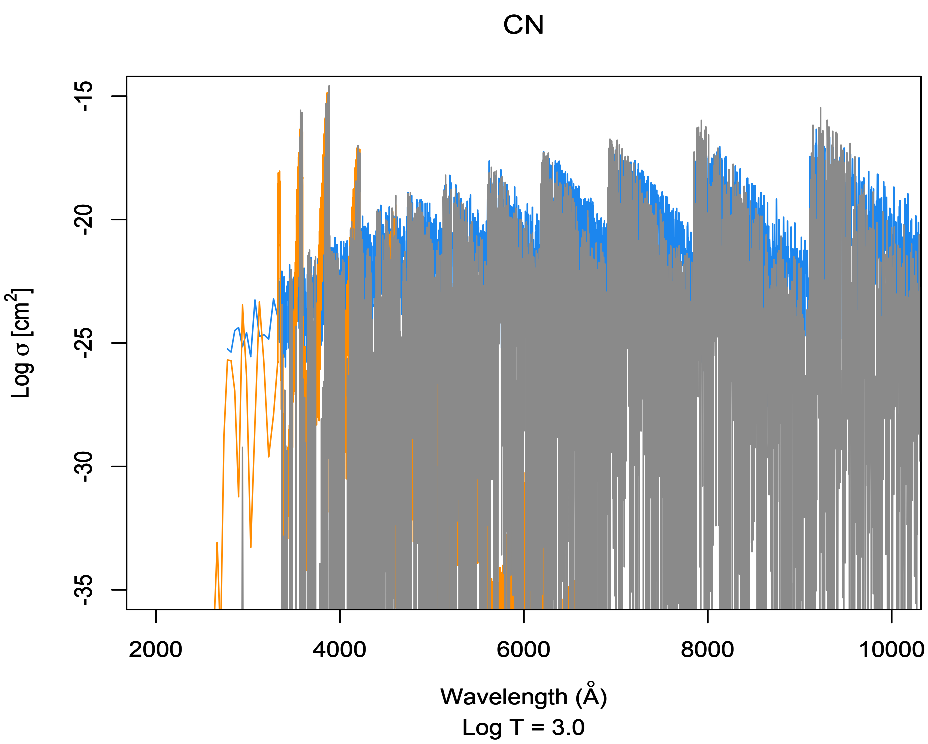

Corresponding colors: ATOP - **Blue**; ExoMol - **Grey**

Figure 7: *CN*: ATOP & ExoMol

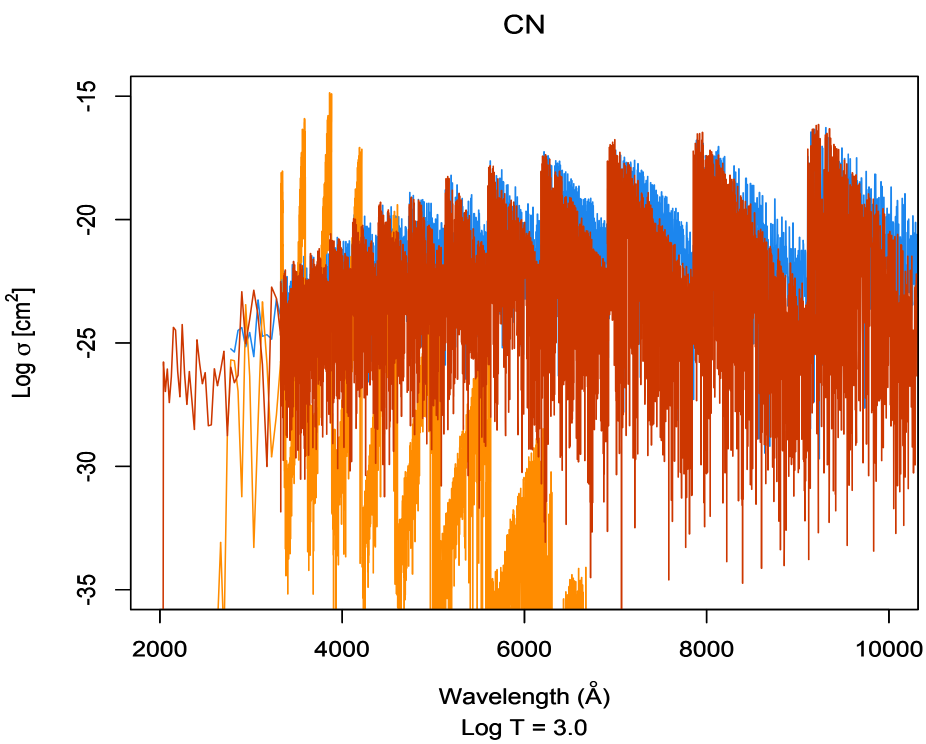

Corresponding colors: ATOP - **Blue**; ATOP Kurucz -**Orange**; PHOENIX Jørgensen - **Red**

Figure 8: *CN*: ATOP & Jørgensen

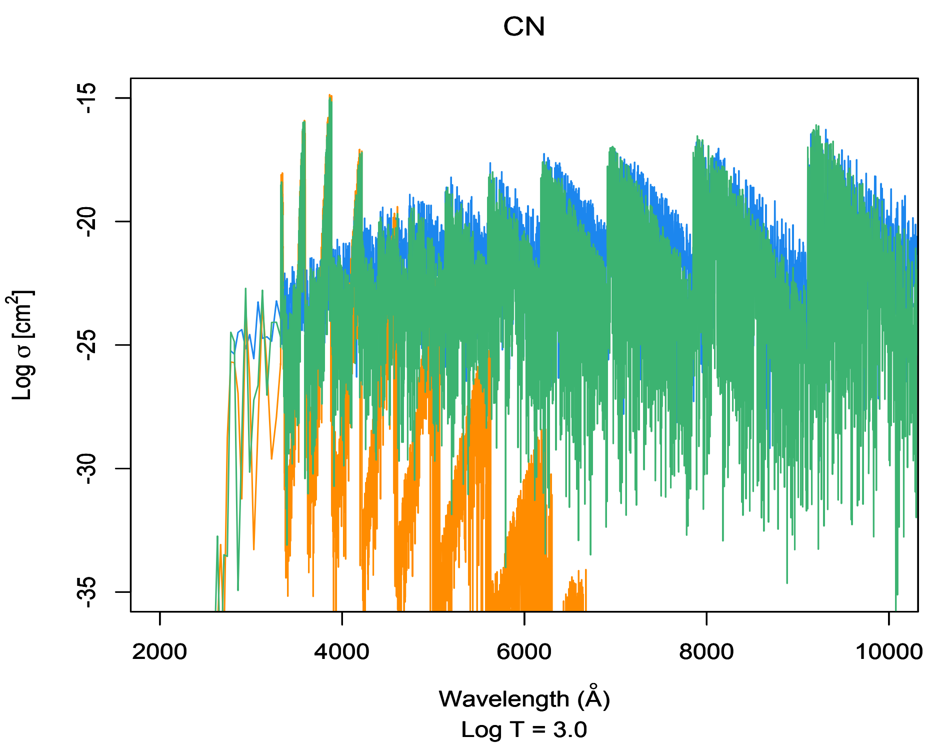

Corresponding colors: ATOP - **Blue**; ATOP Kurucz - **Orange**; PHOENIX Kurucz - **Green**, ExoMol - **Grey**

Figure 9: *CN*: ATOP & Kurucz

4.4 *CO*

The original source from the ATOP code used data from Goorvitch & Chackerian 1994. Line lists were collected from the PHOENIX code, using data from Kurucz 1993 as well as Goorvitch 1994, and Goorvitch & Chackerian 1994a and 1994b. A newer source from VizieR database was also used with a separate data set from Goorvitch 1995.

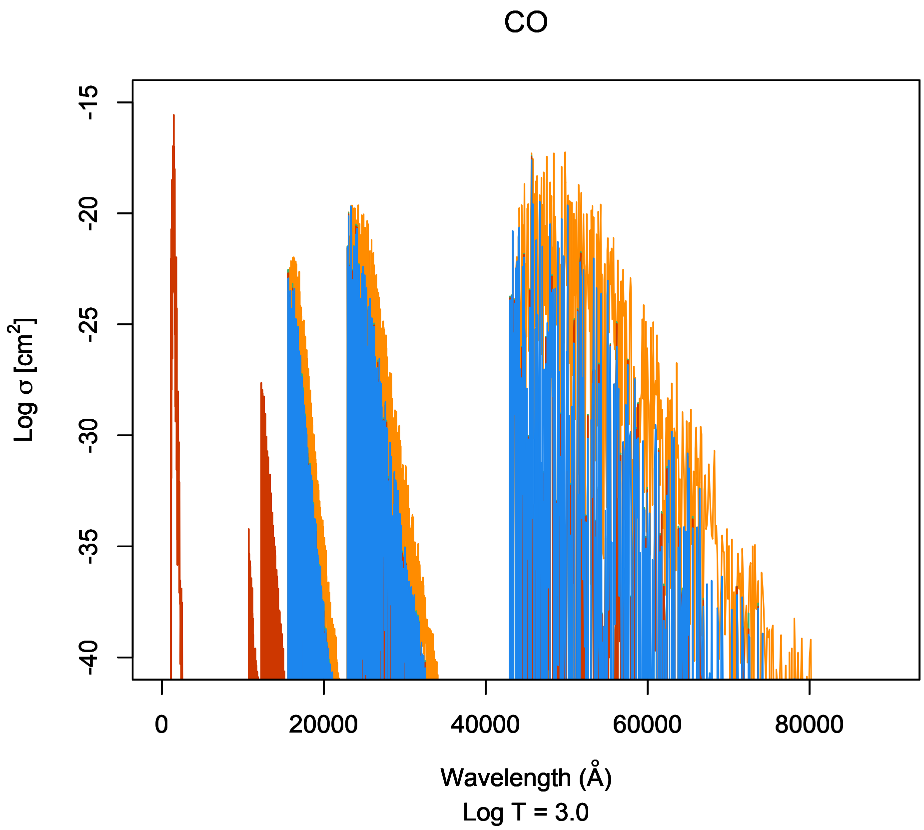

Corresponding colors: ATOP - **Blue**; PHOENIX Goorvitch - **Green**; PHOENIX Kurucz - **Red**; VizieR - **Orange**

Figure 10: *CO*: Full Scale

The full scale graph shows the bands of CO extending out to $80,000$ Å. There is agreement between the three peaks beginning at $20,000$ Å. The ATOP data lies directly below the Goorvitch data, and follow a very similar shape. However, the data from the VizieR, shown in orange, forms an outline above the other two data sets, that is clearly much higher in magnitude than the rest of the sources. The data from Kurucz, in red, also follow the same shape and magnitude of the Goorvitch and ATOP data, although it does display three additional peaks below $15,000$ Å.

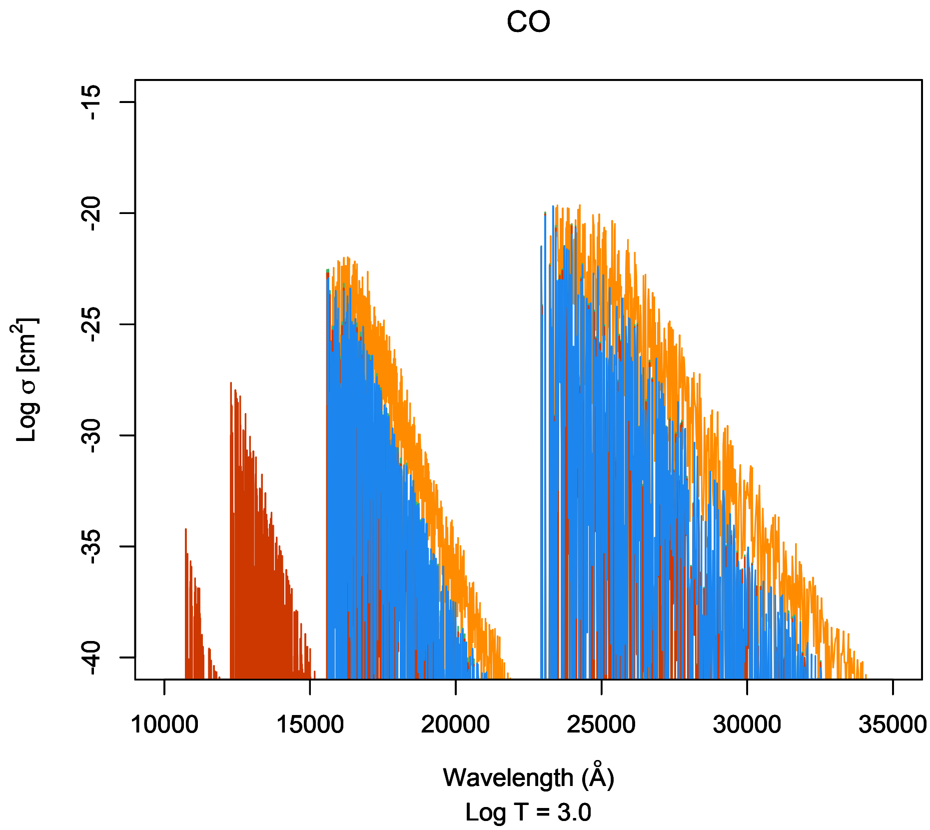

Corresponding colors: ATOP - **Blue**; PHOENIX Goorvitch - **Green**; PHOENIX Kurucz - **Red**; VizieR - **Orange**

Figure 11: CO: Focused

4.5 C_2H_2

Sources for molecular line lists came from a data set from PHOENIX using line lists compiled from HITRAN 1992. A newer dataset with more transitions was collected directly from the HITRAN 2016 database. These were then coupled with partition functions from the HITRAN website. Both molecular sources were compared to the original ATOP cross-sections from Jørgensen 1993.

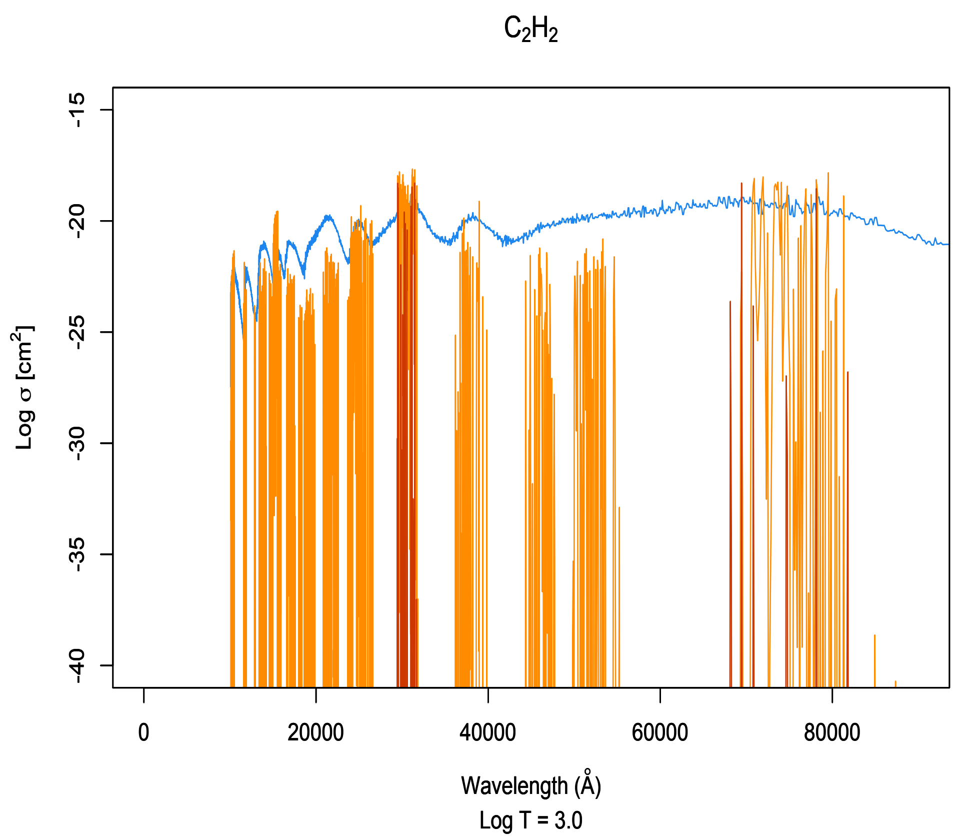

Corresponding colors: ATOP - **Blue**; PHOENIX - **Red**; HITRAN - **Orange**

Figure 12: C_2H_2: Full Scale

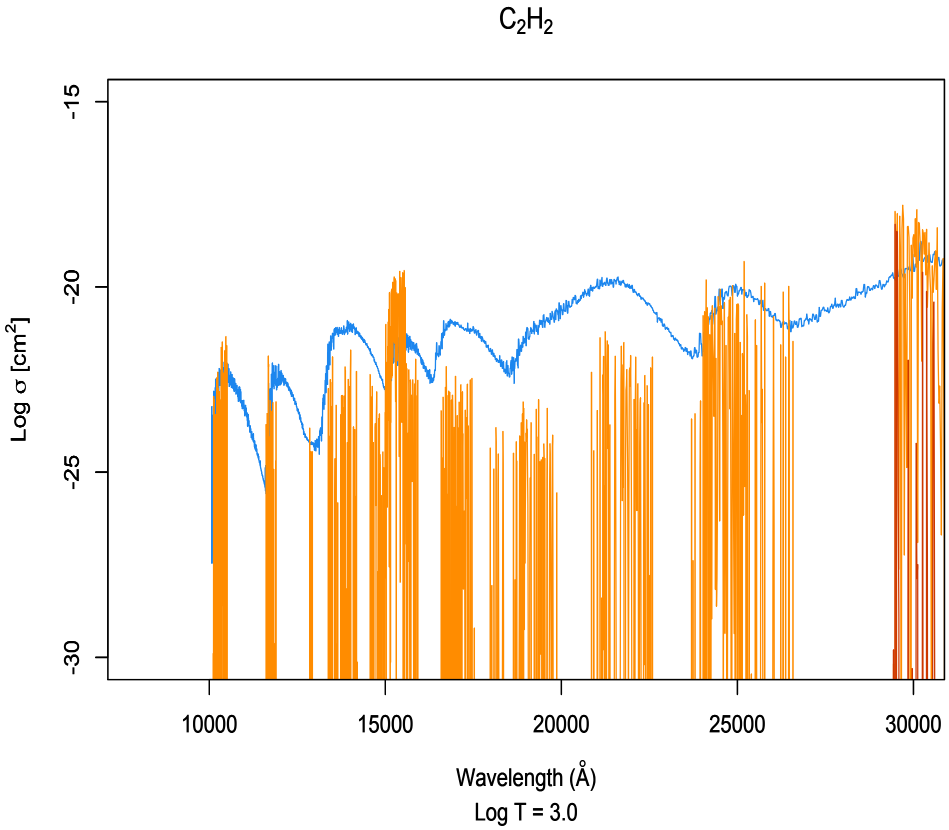

Corresponding colors: Atop - **Blue**; Phoenix - **Red**; HITRAN - **Orange**

Figure 13: C_2H_2: Focused

Though both sources appear to differ, the peaks of the bands follow a similar shape. log σ $[cm^2]$ ranges from -25 to -20 in both sources. The disagreement lies in the shape and width of peaks. The considerable discrepancy is the amount of line transition data from each source. From table (2) HITRAN has $22,000$ transition lines and the Phoenix data contains 1173 transitions while Atop has $10,000,000$ lines. The Phoenix line data is found near $30,000$ Å and fits within the HITRAN band.

4.6 H_2O

Five sources of data were used for molecular absorption of H_2O. PHOENIX data included sources from Miller & Tennyson, from Allard et al. 1994, Ames from Partridge & Schwenke 1997, and Jørgensen et al. 2001. Exomol data originated from Masseron et al 2014. These four sources were then used in comparison to the original ATOP cross-section tables from Jørgensen et al. 1985. The partition function was also included in the line lists from ExoMol.

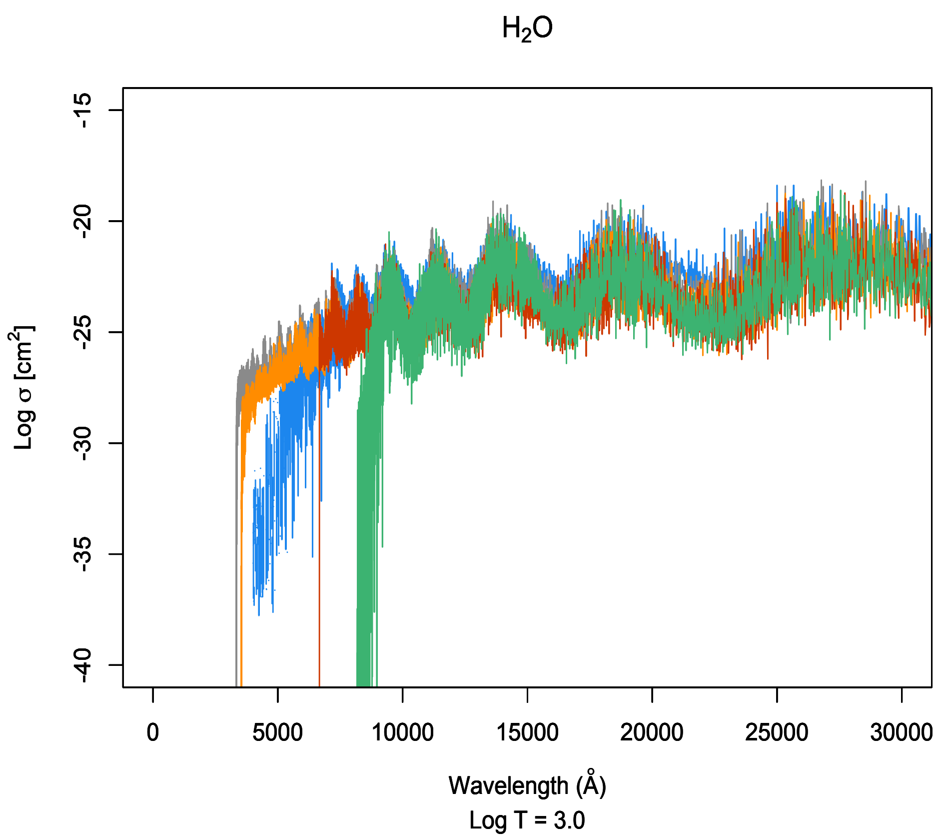

Corresponding colors: ATOP - **Blue**; PHOENIX Ames - **Orange**; PHOENIX Miller & Tennyson - **Green**; PHOENIX Jørgensen - **Red**; ExoMol - **Grey**

Figure 14: H_2O: Focused

Cross-sections of H_2O have well defined peaks that coincide between the five sources. The source from ATOP, as seen in blue, rises slightly higher than the other four sources. In the following figures, the data sources are separated into two groups to display the differences between the newer line lists and the original ATOP data. The most notable distinction in the sources is the starting value, with each having an individual starting with the exception of the ExoMol and Ames data, in grey and orange, respectively. For figure (15), as previously mentioned, is the initial bands of H_2O. The ATOP data does show unusual behavior around 5000 Å, where there is no set structure to the beginning bands. The Jørgensen data, in red, and Miller & Tennyson data, shown in green, show a consensus in magnitude and shape, though the starting values differ slightly. It is clear in the split figures (16), that the Ames and ExoMol data follow a similar shape, though ExoMol continues to be slightly higher.

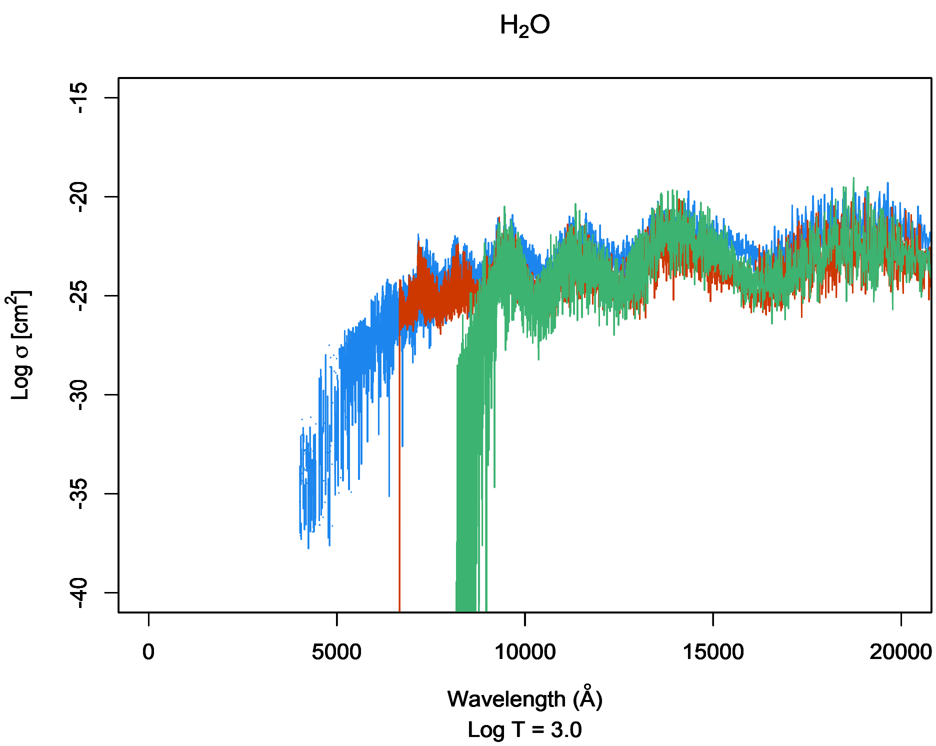

Corresponding colors: ATOP - **Blue**; PHOENIX Jørgensen - **Red**; PHOENIX Miller & Tennyson - **Green**

Figure 15: H_2O: Split 1

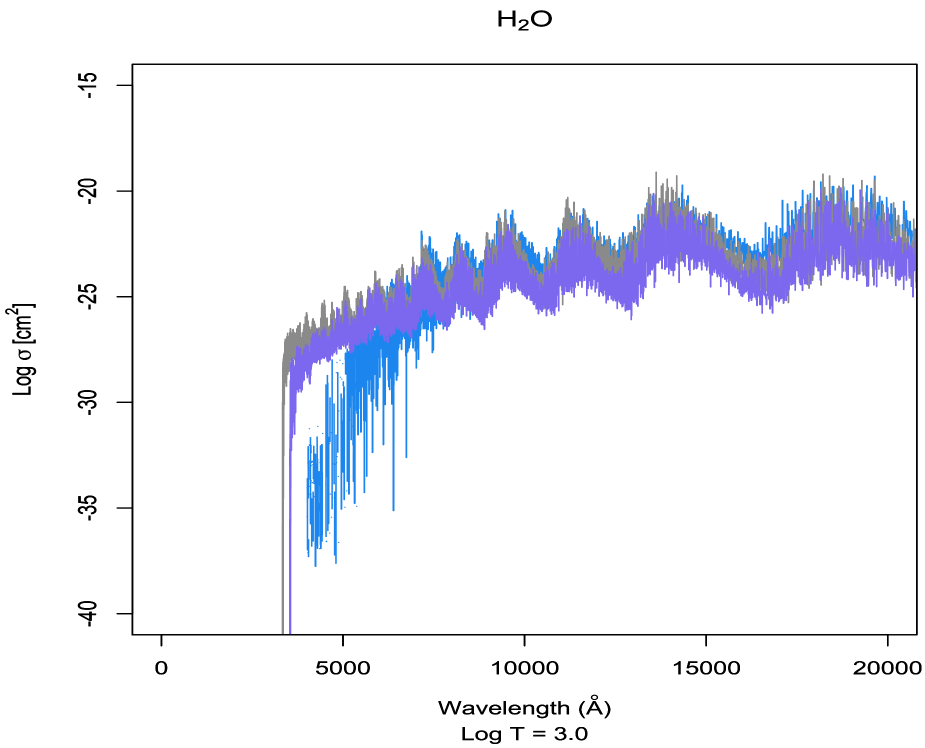

Corresponding colors: ATOP - **Blue**; PHOENIX Ames - **Orange**; ExoMol - **Grey**

Figure 16: H_2O: Split 2

4.7 *HCN*

HCN was compiled using two primary sources. The original source was from Jørgensen et al. 1985 from Atop. The newer source was through ExoMol database, using data from Harris et al. 2006. This source comprised of line list transition files, energy states and a conclusive partition function. Once the data through ExoMol was analyzed, it was then plotted alongside tables from Atop.

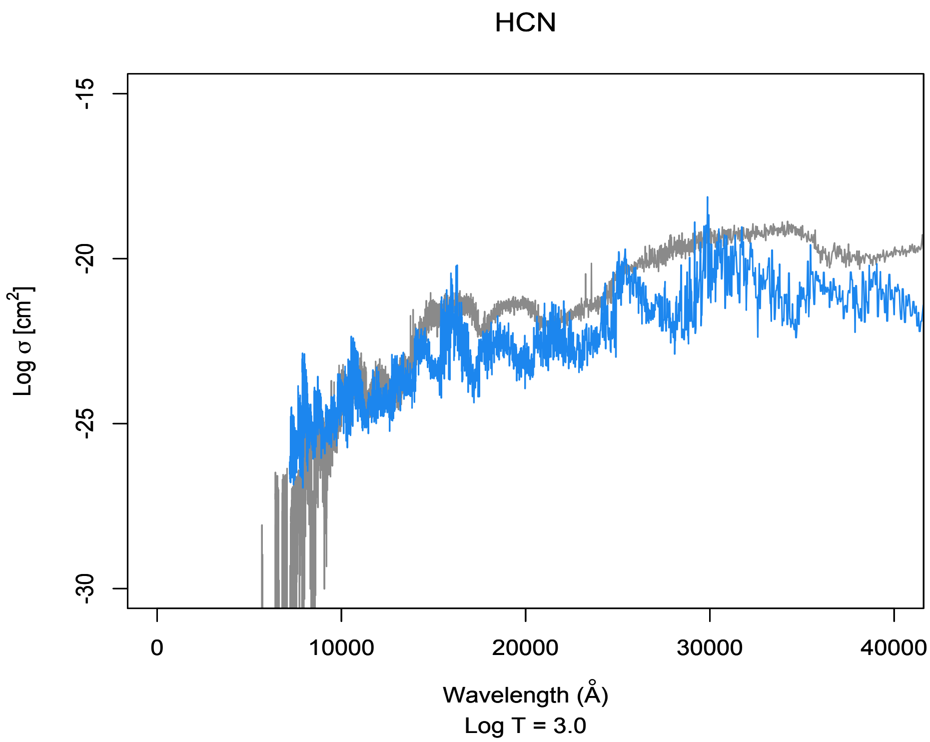

Corresponding colors: Atop - **Blue**; ExoMol - **Grey**

Figure 17: *HCN*: Focused

Within the figure 17, the two sources show a distinction in the band structure. Though there some agreement in magnitude and in some areas, the shape. With the magnitudes of the cross-section remaining somewhat similar, it can be expected to have similar contributions to the opacity.

4.8 *TiO*

TiO was analyzed using two sources of molecular transitions and energy states. One source was from the PHOENIX code, using data from Jørgensen et al. 2001. The second source used data from Ames, by Schwenke & Allard 2000. It was paired with a partition function from the HITRAN database. Once this selection of data was compiled, it was then compared to the original tables from ATOP. The tables from ATOP were compared with data from Jørgensen 1994.

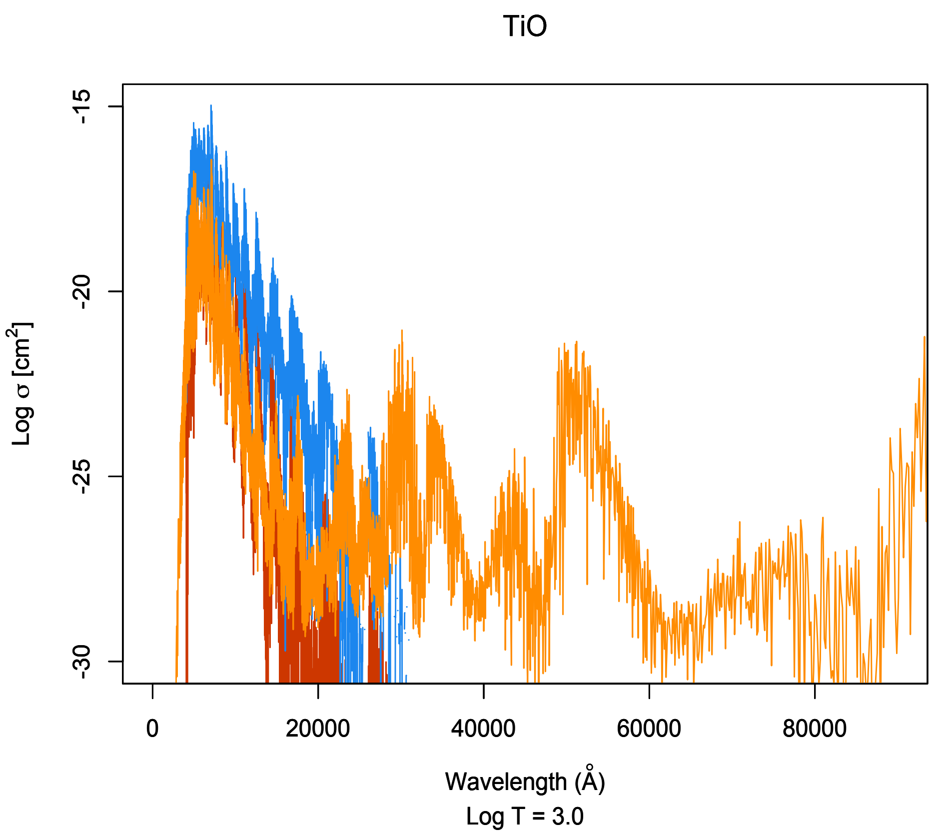

Corresponding colors: ATOP - **Blue**, PHOENIX Jørgensen - **Red**, PHOENIX Ames - **Orange**

Figure 18: *TiO*: Full Scale

The graph of TiO shows a consistent alignment of bands between the three sources. In the focused graph, the peaks for Atop remain above the values for the other two sources. This gives the impression of a higher resulting opacity for Atop. The magnitude of the two Phoenix sources are similar below $10,000$ Å , though the Ames line list drops significantly immediately after. The Phoenix Ames data set continues far into the infrared spectrum.

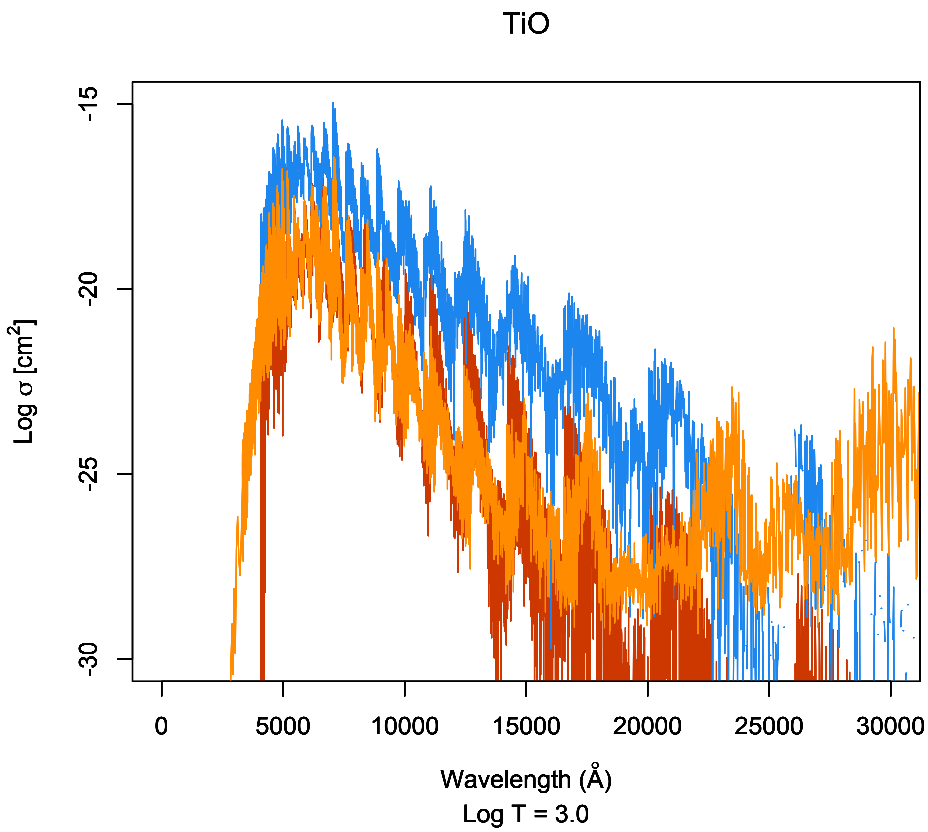

Corresponding colors: Atop - **Blue**, Phoenix Jørgensen - **Red**, Phoenix Ames - **Orange**

Figure 19: TiO: Focused

Chapter Five

5 Mean Opacity Results

The Rosseland mean opacity was calculated using the ATOP and PHOENIX codes. ATOP was used for the calculation with the new molecular line lists, while the PHOENIX calculations are from the original 2005 version. Each figure compares the original opacity from ATOP with PHOENIX and the most recent molecular absorption coefficient calculation using the new ATOP. In addition to the opacities, a zero-line is included. This describes the opacity as if the molecule were excluded from the calculation. The following figures include the mean opacity for both carbon-rich and oxygen rich environments for each molecule over a range of temperatures of $log\ T[K] = 3.0$ to 4.0 with a density parameter of $log\ R = -3.0\ [g\ cm^{-3} K_6^{-3}]$. This density parameter is used to alleviate excess computation time. The density parameter is shown as a fraction of density over a temperature, denoted in millions of Kelvins cubed, $\frac{\rho}{T_6^3}$.

In the oxygen rich environments, both C_2 and CH make very little contribution to the overall opacity, with all sources near the zero line, in figures (21) and (23). However, in the carbon rich environments, it can be seen that C_2 makes a significant difference in opacity. The data from ExoMol rests on the baseline of C_2 and appears to make no significant contributions in comparison to the other sources. The original PHOENIX source appears to be the leading opacity in both molecules, as seen in figures (20) and (22).

In the case of CN and CO, there is virtually no contribution to opacity in oxygen rich environments. Each source lies on the or very near the zero line. For CN, there is a slight elevation for the ATOP data, as seen in figure (25). This is the same in figure (27) for CO. Carbon rich environments show a significant variation in the CN data sources, figure

(24), with Atop and the Phoenix original well above the other sources. The other three sources, Jørgensen, Kurucz and Brooke appear to give no change to the opacity, despite the agreement in the cross-sections, as seen in figure (5) The data for CO show a small contribution to opacity, figure (26), with the Phoenix original opacity slightly above the others.

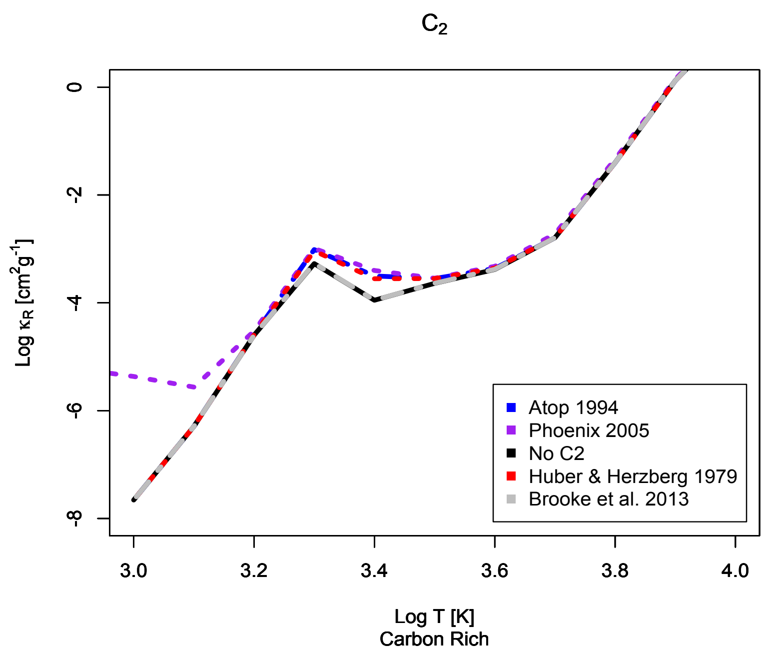

Figure 20: C_2: Carbon Rich

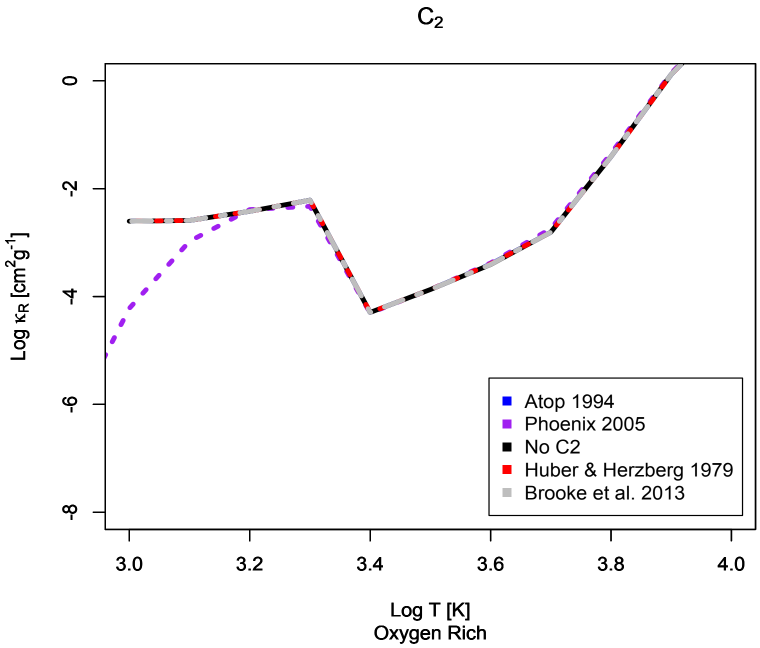

Figure 21: C_2: Oxygen Rich

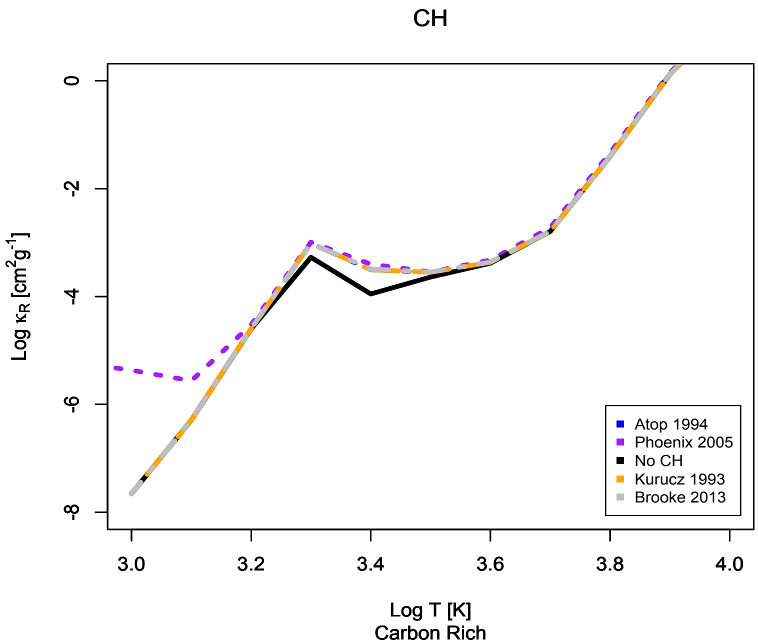

Figure 22: CH: Carbon Rich

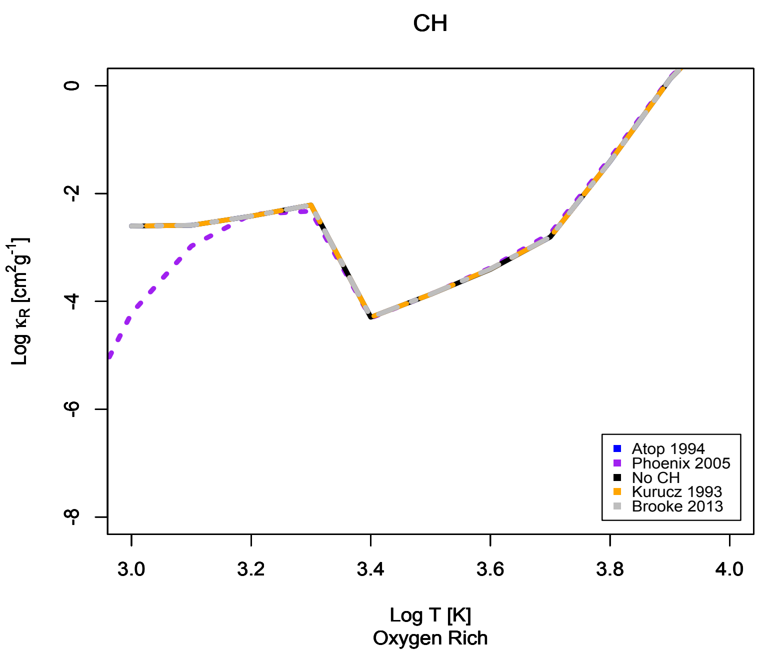

Figure 23: CH: Oxygen Rich

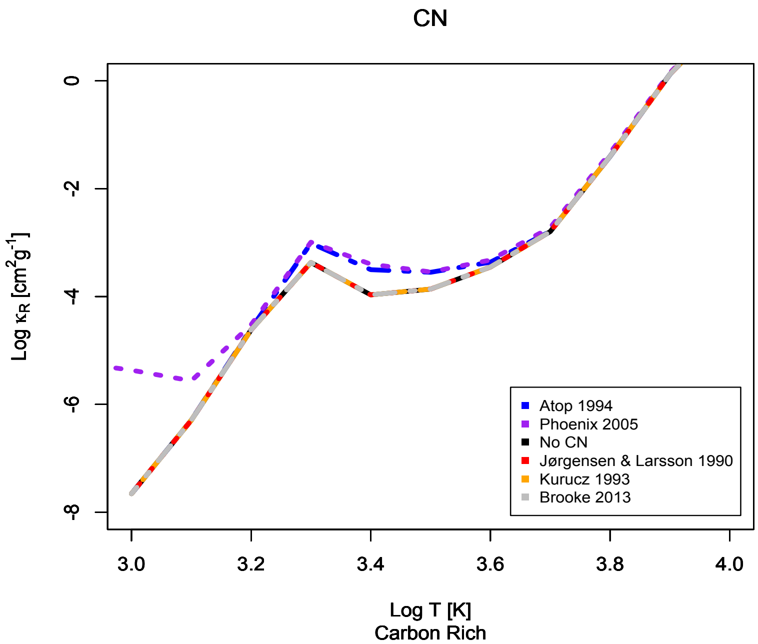

Figure 24: CN: Carbon Rich

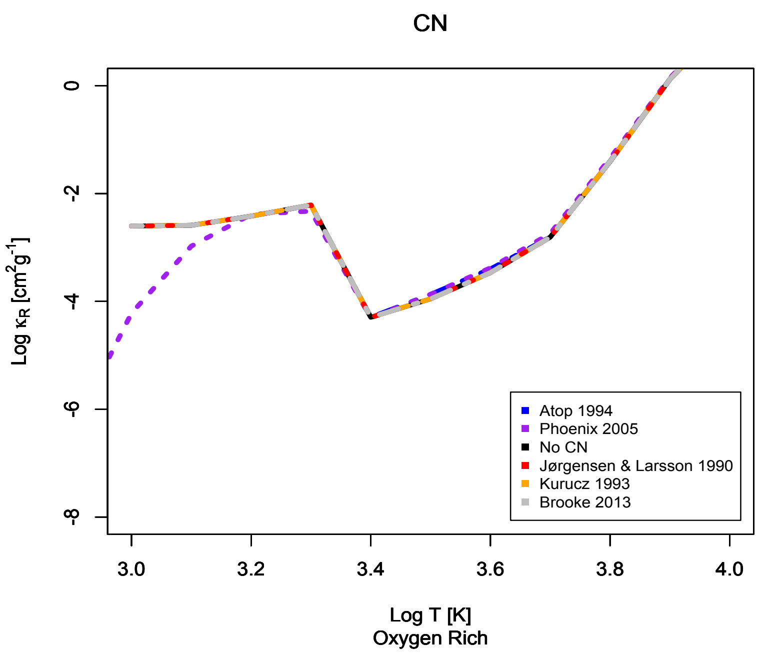

Figure 25: CN: Oxygen Rich

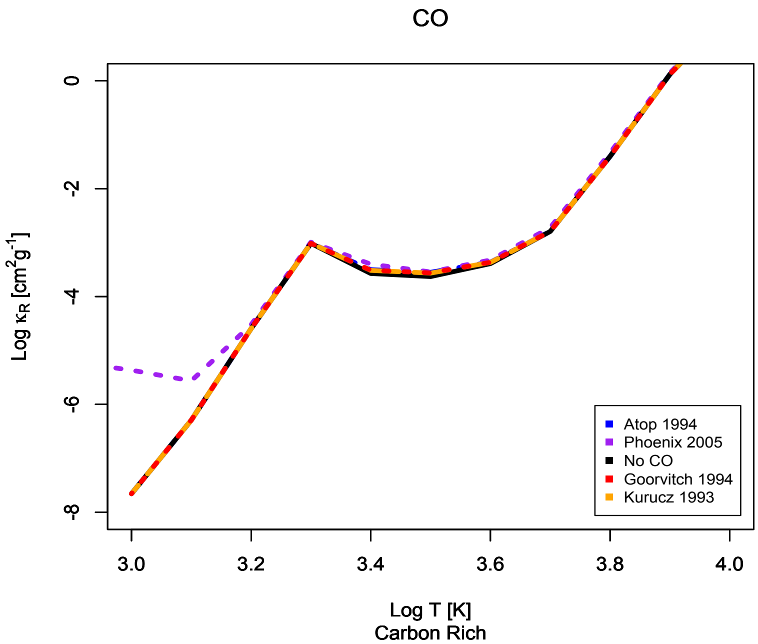

Figure 26: CO: Carbon Rich

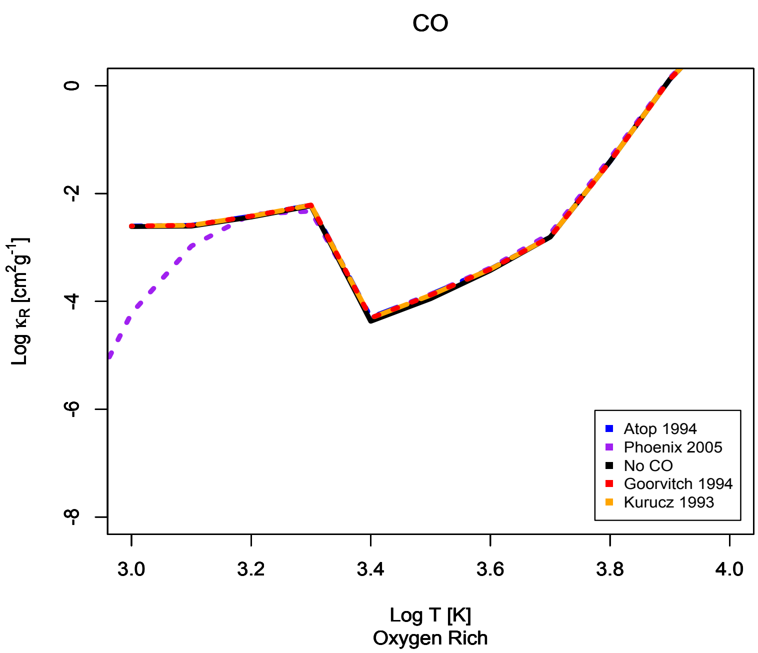

Figure 27: CO: Oxygen Rich

In the oxygen rich environment, the molecule C_2H_2 provides no increase to the mean opacity, figure (29). However, the carbon rich environment does display a change in opacity, with the Atop and Phoenix original lines at at temperature of $log\ T[K] = 3.3$. The other sources of C_2H_2, follow closely to the zero line, as seen in figure (28).

For H_2O, the mean opacity contribution becomes very important in the oxygen rich environments, figure (31). All sources of H_2O follow a very similar shape, with the largest impact to opacity being from ExoMol. In the cross-section figure, (14), there is an overall consensus on magnitude, with ExoMol and Atop varying slightly. Figure (31) displays a wide span of differences in the mean opacity in the lower temperatures. A significant observation to H_2O is the fact that every source contributes to the mean opacity to some degree. Although H_2O makes a major improvement to the opacity in oxygen rich environments, in carbon rich environments, it makes nearly no significant change, figure (30). In the carbon rich figure (30), the Phoenix original becomes the largest contribution to the opacity.

For the carbon rich environment, HCN does alter the mean opacity near the temperature of $log\ T[K] = 3.4$. The ExoMol opacity displays a strange behavior around the lower temperatures, where it increases a few orders of magnitude above the Phoenix original, as seen in figure(32). For figure (33), the contributions to the mean opacity by all sources are on the zero line, and suggest that HCN does not make a significant difference in oxygen rich environments. For TiO, the contributions in oxygen rich environments are significant around $log\ T[K] = 3.3$, see figure (35). There is a variation in mean opacity between sources, though there is a corresponding shape that remains consistent. Both the Atop and Phoenix original mean opacities make the most significant contribution in comparison to the other sources. Within the carbon rich environments, TiO, makes very little impact on the overall mean opacity, as seen in figure (34).

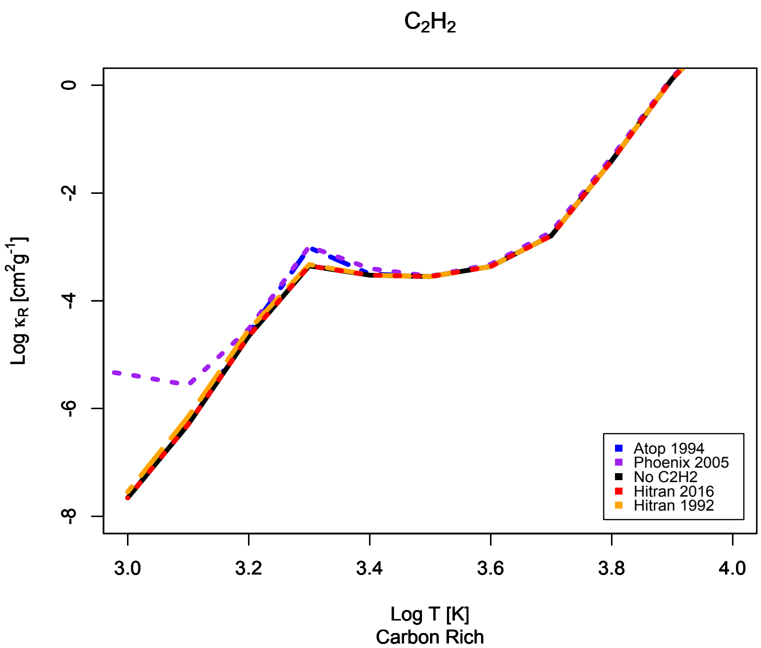

Figure 28: C_2H_2: Carbon Rich

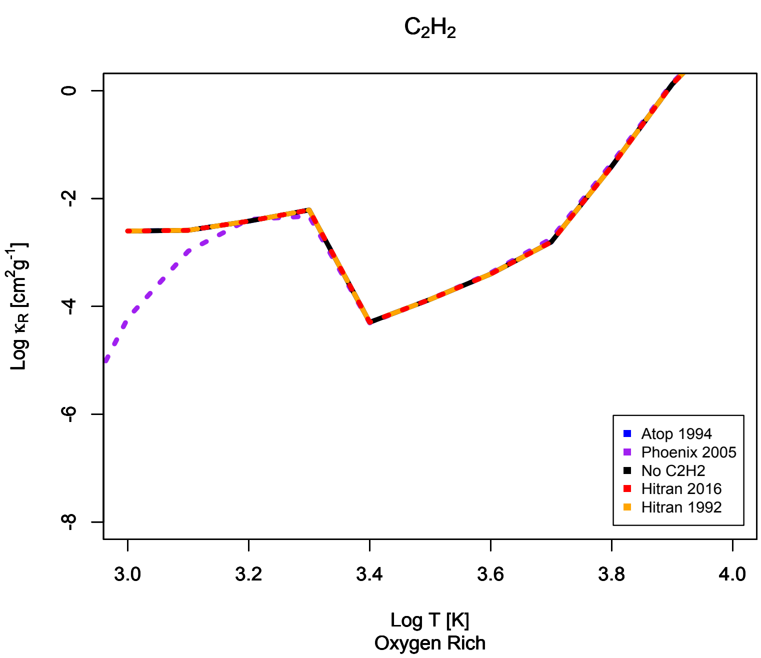

Figure 29: C_2H_2: Oxygen Rich

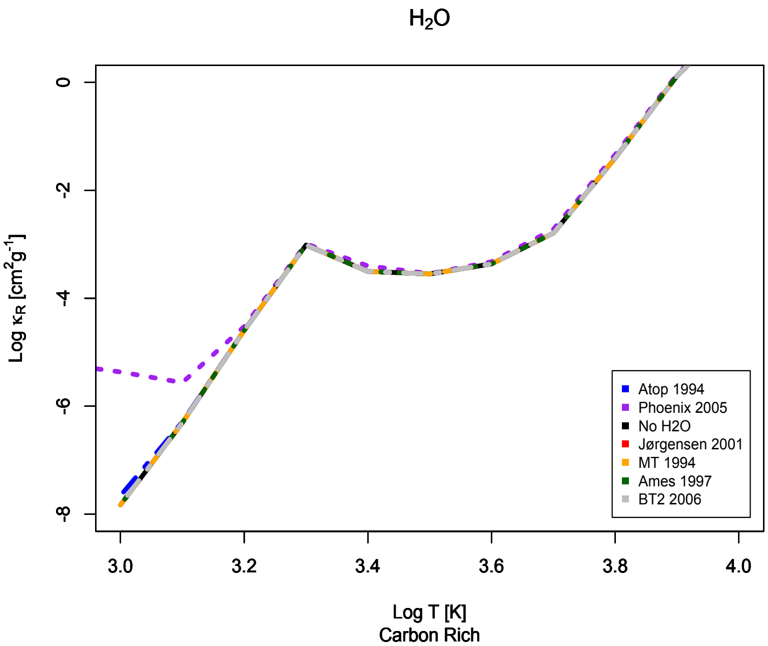

Figure 30: H_2O: Carbon Rich

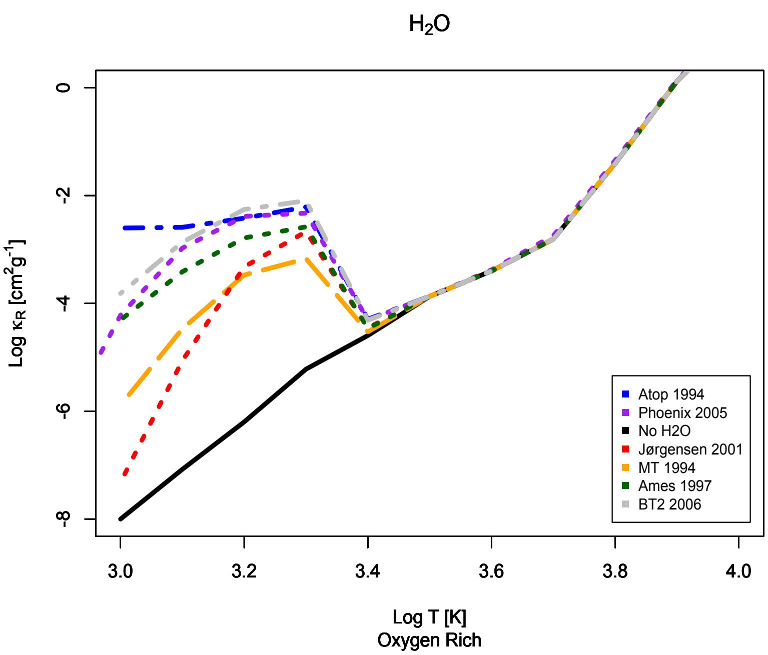

Figure 31: H_2O: Oxygen Rich

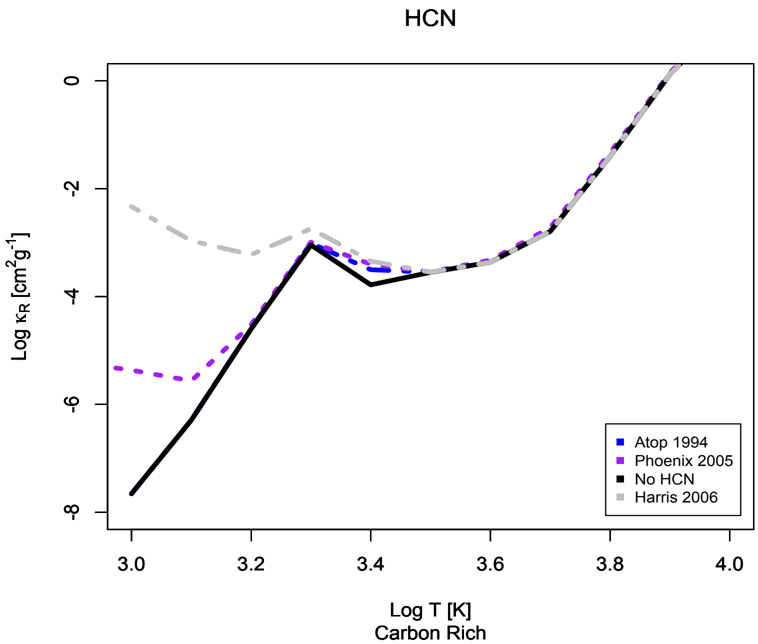

Figure 32: HCN: Carbon Rich

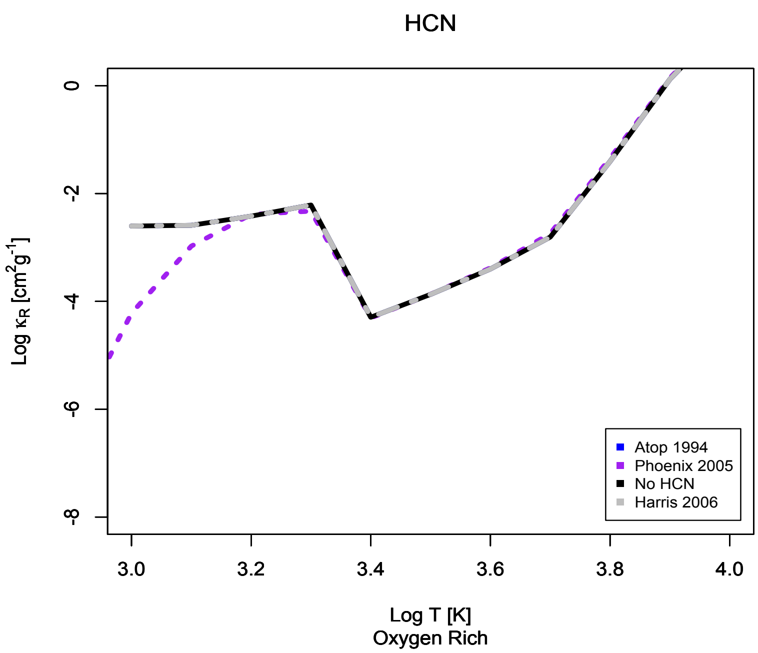

Figure 33: HCN: Oxygen Rich

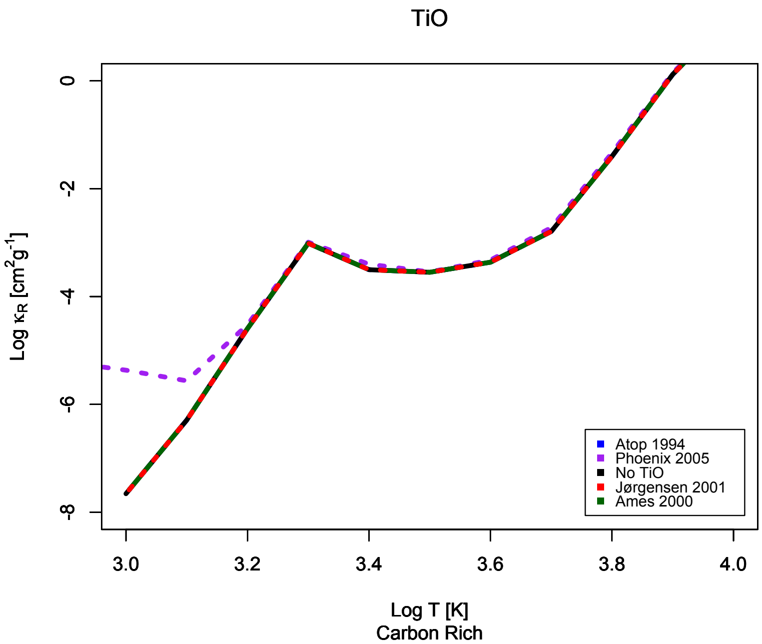

Figure 34: TiO: Carbon Rich

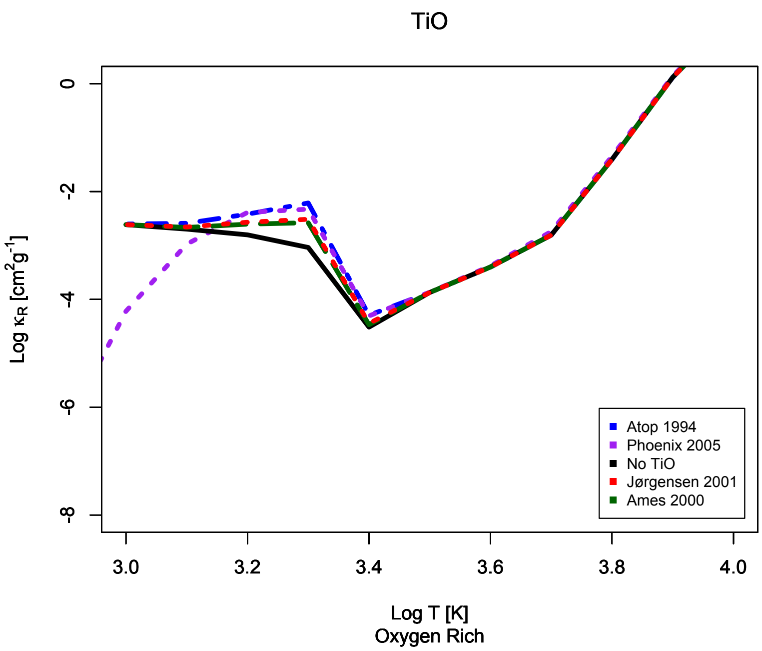

Figure 35: TiO: Oxygen Rich

6 Discussion

For a range of carbon to oxygen ratios in stellar atmospheres, various molecular absorbers can become significant. Three figures will be introduced of Rosseland mean opacity as a function of temperature, in each in a different carbon-oxygen ratio environment. Similar to the previous figures displaying the Rosseland mean opacity for each molecule, see Chapter 5, the opacities are plotted with the density parameter $log\ R = -3.0\ [g\ cm^{-3} K_6^{-3}]$. The four sources in the figures include the original ATOP code, the updated ATOP code, the PHOENIX code, and the ÆSOPUS code, designated as Marigo hereafter [26].

From the molecular absorption cross-sections calculated in Chapter 4, a more updated list of absorbers was assembled for the new ATOP. A complete list of molecular data chosen for the updated ATOP code can be seen in the following table (3).

Table 3: **Atop Molecular Absorber Data Update**

Molecule	Data Source
C_2	Sharp 1984
CH	Masseron et al 2014
CN	Brooke et al. 2014
CO	Goorvitch & Chackerian 1994
C_2H_2	Hitran 2016
HCN	Harris et al. 2006
H_2O	Barber et al. 2006
TiO	Jørgensen et al. 2001

6.1 Oxygen Rich

In an oxygen rich environment, there tends to be a mix of carbon and oxygen forming CO, and an excess of oxygen that tends to form molecules like H_2O, and TiO. These molecules play a key role in the opacity at certain temperatures. For molecules like water, the influence in opacity occurs at lower temperatures, around $log\ T[K] = 3.2$

In the figure (36), the opacity trend is seen in an oxygen rich environment. Towards the higher temperatures, greater than $log\ T[K] = 3.7$, the opacity sources are dominated by hydrogen. In the middle, around $log\ T[K] = 3.6$, small molecules begin to contribute. It begins a slight difference in sources, as the temperature is followed from right to left. As the opacity begins to drop, as the temperature is lowered, it can be seen that there is a large trend upwards around $log\ T[K] = 3.3$. This significant increase in opacity is shown by all sources, and is caused by the contribution of H_2O. Marigo shows a greater abundance of water within the code that causes the larger overall increase to opacity. If temperature is decreased further, the original Atop, shown in green, stops in the code, and displays the incorrect behavior. The drop in opacity, as shown by the updated Atop code and the Phoenix code, is an expected trend in the lower temperatures. As the temperature decreases, most molecules have the tendency to be in the ground state, becoming increasingly difficult to transition to the upper energy levels.

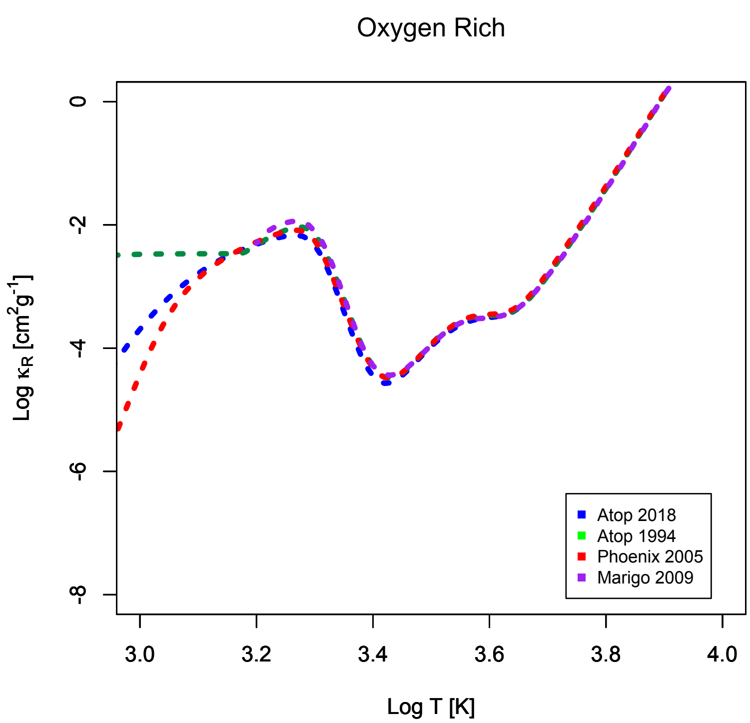

Figure 36: κ_R: C/O = 0.49, Oxygen Rich

6.2 Equal Amounts of Carbon and Oxygen

The following figure shows each opacity calculation in a carbon-oxygen ratio of a typical normal sized star, like the Sun. In the higher temperatures, the opacity is influenced mainly by hydrogen. As the temperature reaches $log\ T[K] = 3.6$, small molecules vary the opacity slightly, even as the magnitude decreases. There is a significant difference beginning at $log\ T[K] = 3.3$, where the updated ATOP code rises, and the original ATOP and PHOENIX decline. The Marigo data shows an apparent upward shift, similar to the new ATOP.

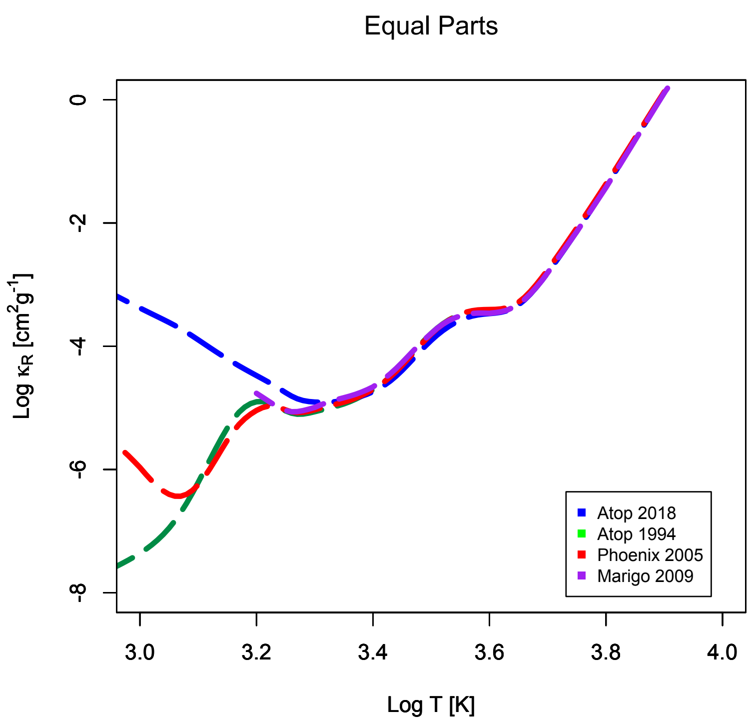

Figure 37: κ_R: C/O = 1.0

6.3 Carbon Rich

Just as in the oxygen rich environment, the carbon rich environment tends to produce CO. However, with an excess of carbon, more molecules like C_2, CN, and HCN begin to contribute as absorbers. In figure (38), much like the oxygen rich environment, the higher temperatures are dominated largely in part by hydrogen. As the temperature decreases, between $log\ T[K] = 3.6$ to $log\ T[K] = 3.4$, there is a decline in opacity that is shown by each source. There is a significant difference between opacity in each of the sources near $log\ T[K] = 3.3$. Marigo has a trend upwards, as both the original Atop code and Phoenix code have a large decrease in opacity. At this point there is a dramatic change between sources. The updated Atop code shows a slight decrease, and then an upward trend. This is quite possibly from the addition of HCN to the new Atop code. Referring back to figure (32), the contribution by Harris to opacity, is substantial in comparison to all other sources at the lower temperatures.

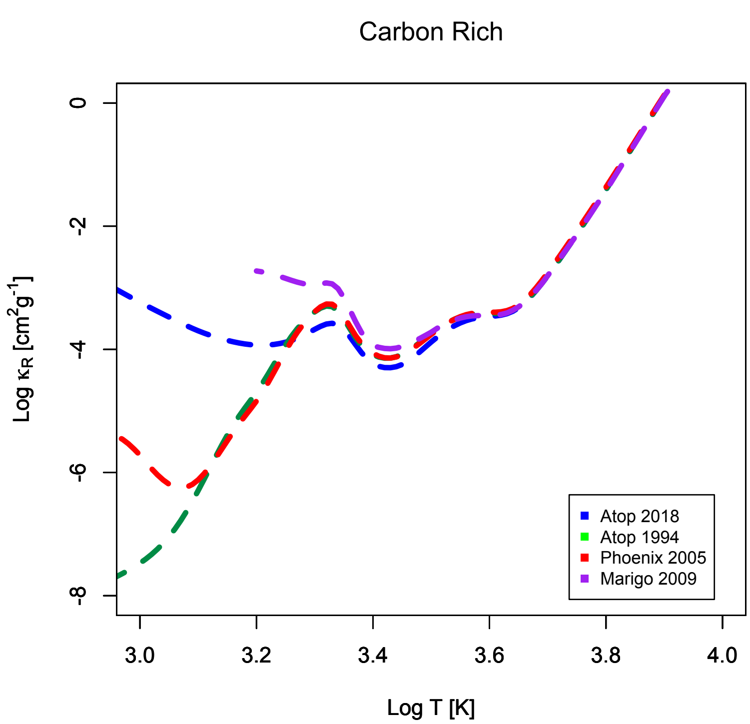

Figure 38: κ_R: C/O = 1.1, Carbon Rich

6.4 Future Studies

Though the calculations done here were just a small part of the inner workings of a star, it leads to a more accurate description of the mean opacity. This study will eventually be apart of the comprehensive upgrade to the ATOP code. The opacity tables produced here, can then be used to create more precise models of stellar evolution. The overall consensus in figures (36, 37, 38) show a reasonable validity in the method used to update the ATOP code.

REFERENCES

REFERENCES

[1] Alexander, D. R., and Ferguson, J. W. Low-temperature Rosseland opacities. *Astrophysical Journal Supplement Series 437* (Dec 1994), 879–891.

[2] Allard, F., Hauschildt, P. H., Miller, S., and Tennyson, J. The influence of h2o line blanketing on the spectra of cool dwarf stars. *The Astrophysical Journal 426* (May 1994), L39–L41.

[3] Allard, F., Hauschildt, P. H., and Schwenke, D. Tio and h2o absorption lines in cool stellar atmospheres. *The Astrophysical Journal 540*, 2 (Sep 2000), 1005–1015.

[4] Barber, R. J., Strange, J. K., Hill, C., Polyansky, O. L., Mellau, G. C., Yurchenko, S. N., and Tennyson, J. Exomol line lists – iii. an improved hot rotation-vibration line list for hcn and hnc. *Monthly Notices of the Royal Astronomical Society 437*, 2 (2014), 1828–1835.

[5] Barber, R. J., Tennyson, J., Harris, G. J., and Tolchenov, R. N. A high-accuracy computed water line list. *Monthly Notices of the Royal Astronomical Society 368*, 3 (2006), 1087–1094.

[6] Barklem, P. S., and Collet, R. VizieR Online Data Catalog: Partition Functions for Molecules and Atoms (Barklem+, 2016). *VizieR Online Data Catalog 358* (Feb 2016), 1–12.

[7] Brooke, J. S. A., Bernath, P. F., Western, C. M., Schmidt, T. W., Bacskay, G. B., van Hemert, M. C., and Groenenboom, G. C. New Line Lists Including Intensities for the {C_2} Swan System (d^3Π{_g}-a^3Π{_u}), {C_2} Singlet Systems and Rovibrational Transitions Within the NH X^3Σ{^-} Ground State. In *68th International Symposium on Molecular Spectroscopy* (June 2013).

[8] Brooke, J. S. A., Ram, R. S., Western, C. M., Li, G., Schwenke, D. W., and Bernath, P. F. Einstein a coefficients and oscillator strengths for the a 2pi-x 2sigma+ (red) and b2sigma+-x2sigma+ (violet) systems and rovibrational transitions in the x 2sigma+ state of cn. *The Astrophysical Journal Supplement Series 210*, 2 (2014), 23.

[9] Böhm-Vitense, E. *Introduction to Stellar Astrophysics:*. Introduction to Stellar Astrophysics. Cambridge University Press, 1989.

[10] Chase, M. W., Wang, L., and Blakeslee, D. M. *NIST JANAF Thermochemical tables Shomate Coefficients Database*. NIST Publications, 1997.

[11] Cox, A. N. *Allen's astrophysical quantities.* New York: AIP Press; Springer, 2000, 2000.

[12] Ferguson, J. W., Alexander, D. R., Allard, F., Barman, T., Bodnarik, J. G., Hauschildt, P. H., Heffner-Wong, A., and Tamanai, A. Low-Temperature Opacities. *The Astrophysical Journal 623*, 1 (2005), 585.

[13] Goorvitch, D. Infrared CO line for the X 1 Sigma(+) state. *Astrophysical Journal Supplement Series 95* (Dec 1994), 535–552.

[14] Goorvitch, D. VizieR Online Data Catalog: Infrared CO line list for X 1Σ+ state (Goorvitch, 1994). *VizieR Online Data Catalog 209* (Feb. 1995), 535–552.

[15] Goorvitch, D., and Chackerian, Jr., C. Rovibrational intensities of the minor isotopes of the co x^{1}. 1458.

[16] Gordon, I., Rothman, L., Hill, C., Kochanov, R., Tan, Y., Bernath, P., Birk, M., Boudon, V., Campargue, A., Chance, K., Drouin, B., Flaud, J.-M., Gamache, R., Hodges, J., Jacquemart, D., Perevalov, V., Perrin, A., Shine, K., Smith, M.-A., Tennyson, J., Toon, G., Tran, H., Tyuterev, V., Barbe, A., Császár, A., Devi, V., Furtenbacher, T., Harrison, J., Hartmann, J.-M., Jolly, A., Johnson, T., Karman, T., Kleiner, I., Kyuberis, A., Loos, J., Lyulin, O., Massie, S., Mikhailenko, S., Moazzen-Ahmadi, N., Müller, H., Naumenko, O., Nikitin, A., Polyansky, O., Rey, M., Rotger, M., Sharpe, S., Sung, K., Starikova, E., Tashkun, S., Auwera, J. V., Wagner, G., Wilzewski, J., Wcisło, P., Yu, S., and Zak, E. The hitran 2016 molecular spectroscopic database. *Journal of Quantitative Spectroscopy and Radiative Transfer 203* (2017), 3 – 69. HITRAN2016 Special Issue.

[17] Harris, G. J., Tennyson, J., Kaminsky, B. M., Pavlenko, Y. V., and Jones, H. R. A. Improved hcn/hnc linelist, model atmospheres and synthetic spectra for wz cas. *Monthly Notices of the Royal Astronomical Society 367*, 1 (2006), 400–406.

[18] Huber, K. P., and Herzberg, G. *Constants of Diatmoic Molecules.* Van Bostrand Reinholt, 1979.

[19] Jorgensen, U. G., and Jensen, P. The Dipole Moment Surface and the Vibrational Transition Moments of H_2O. *Journal of Molecular Spectroscopy 161* (Sep 1993), 219–242.

[20] Jorgensen, U. G., Jensen, P., and Sorensen, G. O. H2O in stellar atmospheres. 51.

[21] Jørgensen, U. G. Effects of tio in stellar atmospheres. *Astronomy and Astrophysics 284* (Apr 1994), 179–186.

[22] Jørgensen, U. G., Almlöf, J., Gustafsson, B., Larsson, M., and Siegbahn, P. Casscf and cci calculations of the vibrational band strengths of hcn. *The Journal of Chemical Physics 83*, 6 (1985), 3034–3041.

[23] Jørgensen, U. G., Jensen, P., Sørensen, G. O., and Aringer, B. H2o in stellar atmospheres. *Astronomy & Astrophysics 372*, 1 (2001), 249–259.

[24] Jørgensen, U. G., and Larsson, M. Molecular opacities of astrophysical interest - the a2pi-x2sigma( ) system of cn. *Astronomy and Astrophysics 238* (Nov 1990), 424–434.

[25] Li, G., Gordon, I., Rothman, L., Tan, Y., Hu, S.-M., Kassi, S., Campargue, A., and Medvedev, E. Rovibrational line lists for nine isotopologues of the co molecule in the x$^1/sigma^+$ ground electronic state. *Astrophys. J. Suppl. Ser. 216* (2015).

[26] Marigo, P., and Aringer, B. Low-temperature gas opacity. ÆSOPUS: a versatile and quick computational tool. *Astronomy and Astrophysics 508* (dec 2009), 1539–1569.

[27] Masseron, T., Plez, B., Eck, S. V., Colin, R., Daoutidis, I., Godefroid, M., Coheur, P.-F., Bernath, P., Jorissen, A., Christlieb, N., and et al. Ch in stellar atmospheres: An extensive linelist. *Astronomy & Astrophysics 571* (2014).

[28] Mihalas, D. *Stellar Atmospheres.* Astronomy and Astrophysics Series. W. H. Freeman, 1978.

[29] Novotny, E. *Introduction to Stellar Atmospheres and Interiors.* Oxford University Press, 1973.

[30] PARTRIDGE, H., AND SCHWENKE, D. W. The determination of an accurate isotope dependent potential energy surface for water from extensive ab initio calculations and experimental data. *The Journal of Chemical Physics 106*, 11 (1997), 4618–4639.

[31] ROTHMAN, L., GAMACHE, R., TIPPING, R., RINSLAND, C., SMITH, M., BENNER, D., DEVI, V., FLAUD, J.-M., CAMY-PEYRET, C., PERRIN, A., GOLDMAN, A., MASSIE, S., BROWN, L., AND TOTH, R. The hitran molecular database: Editions of 1991 and 1992. *Journal of Quantitative Spectroscopy and Radiative Transfer 48*, 5 (1992), 469 – 507. Special Issue Conference on Molecular Spectroscopic Databases.

[32] RYDEN, B., AND PETERSON, B. *Foundations of Astrophysics*. Addison-Wesley, 2010.

[33] SHARP, C. M. The computation of franck-condon factors, r-centroids and associated quantities in the electronic transitions of diatomic molecules. *Astronomy & Astrophysics 55* (Jan 1984), 33–50.

[34] TENNYSON, J., YURCHENKO, S. N., AL-REFAIE, A. F., BARTON, E. J., CHUBB, K. L., COLES, P. A., DIAMANTOPOULOU, S., GORMAN, M. N., HILL, C., LAM, A. Z., LODI, L., MCKEMMISH, L. K., NA, Y., OWENS, A., POLYANSKY, O. L., SOUSA-SILVA, C., UNDERWOOD, D. S., YACHMENEV, A., AND ZAK, E. The ExoMol database: Molecular line lists for exoplanet and other hot atmospheres. *Journal of Molecular Spectroscopy 327* (Sep 2016), 73–94. arXiv: 1603.05890.